

SKB

**TECHNICAL
REPORT**

97-16

**Groundwater flow through
a natural fracture**

**Flow experiments and numerical
modelling**

Erik Larsson

Dept. of Geology, Chalmers University of Technology,
Göteborg, Sweden

September 1997

SVENSK KÄRNBRÄNSLEHANTERING AB
SWEDISH NUCLEAR FUEL AND WASTE MANAGEMENT CO

P.O.BOX 5864 S-102 40 STOCKHOLM SWEDEN
PHONE +46 8 459 84 00
FAX +46 8 661 57 19

GROUNDWATER FLOW THROUGH A NATURAL FRACTURE

FLOW EXPERIMENTS AND NUMERICAL MODELLING

Erik Larsson

**Dept. of Geology, Chalmers University of Technology,
Göteborg, Sweden**

September 1997

This report concerns a study which was conducted for SKB. The conclusions and viewpoints presented in the report are those of the author(s) and do not necessarily coincide with those of the client.

Information on SKB technical reports from 1977-1978 (TR 121), 1979 (TR 79-28), 1980 (TR 80-26), 1981 (TR 81-17), 1982 (TR 82-28), 1983 (TR 83-77), 1984 (TR 85-01), 1985 (TR 85-20), 1986 (TR 86-31), 1987 (TR 87-33), 1988 (TR 88-32), 1989 (TR 89-40), 1990 (TR 90-46), 1991 (TR 91-64), 1992 (TR 92-46), 1993 (TR 93-34), 1994 (TR 94-33), 1995 (TR 95-37) and 1996 (TR 96-25) is available through SKB.

GROUNDWATER FLOW THROUGH A NATURAL FRACTURE

FLOW EXPERIMENTS AND NUMERICAL MODELLING

Erik Larsson, Department of Geology, Chalmers University of Technology,
S-412 96 Göteborg, Sweden.

970918

Keywords: rock fracture, hydraulic properties, aperture measurements,
numerical modeling, flow experiments, two-phase flow.

ABSTRACT (ENGLISH)

Groundwater flow and transport play an important role not only for groundwater exploration but also in environmental engineering problems. This report considers how the hydraulic properties of fractures in crystalline rock depend on the fracture aperture geometry.

Different numerical models are discussed and a FDM computer code for two- and three-dimensional flow-modelling has been developed. Different relations between the cells in the model are tested and compared with results in the literature.

A laboratory experimental work has been done to carry out flow experiments and aperture measurements on the same specimen of a natural fracture. The drilled core sample had fractures parallel to the core axis and was placed inside a biaxial cell during the experiments. The water pressure gradient and the compression stress were varied during the experiments and also a tracer test was done. After the flow experiments, the aperture distribution for a certain compression was measured by injecting an epoxy resin into the fracture. The thickness of the resin layer was then studied in saw cut sections of the sample. The results from the experiments were used to validate numerical and analytical models, based on aperture distribution, for flow and transport simulations.

In the disturbed zone around a drift both water and air are present in the fractures. The gas will go to the most wide part of the fracture because the capillarity and the conductivity decrease. The dependence of the effective conductivity on the variance of the conductivity and the effect of extinction of highly conductive cells has also been studied. A discussion of how gas in fractures around a drift can cause a skin effect is modelled and an example is given of what a saturation depending on the magnitude of the flow causes.

ABSTRACT (SWEDISH)

Flöde och transport av grundvatten är viktigt inte bara för exploatering av grundvatten utan också i andra miljömässiga ingenjörproblem. Den här rapporten behandlar hur de hydrauliska faktorerna hos sprickor i kristallint berg beror på sprickviddsgeometrin.

Olika numeriska modeller diskuteras och ett FDM-program för två- och tredimensionell flödesmodellering har utvecklats. Olika förhållanden mellan cellerna i modellen har testats och jämförts med resultat funna i litteraturen.

Ett laboratorieförsök har genomförts där flödesexperiment och mätningar av sprickvidden har gjorts på samma naturliga spricka. Den utborrade bergskärnan som användes hade sprickor parallellt med kärnans längdaxel och placerades i en biaxialcell under försöken. Den pålagda hydrauliska gradienten över sprickan och kompressionstrycket varierades under provets gång och även ett språrämnesförsök genomfördes. Efter flödesförsöken mättes sprickviddsfördelningen vid ett visst kompressionstryck genom att epoxy injekterades och fick härda i sprickan. Epoxyskiktets tjocklek studerades sedan i sågade sektioner av sprickprovet. Resultaten från försöken användes till att validera numeriska och analytiska beräkningsmodeller baserade på sprickviddsfördelning för flödes- och transportsimuleringar.

I den störda zonen kring en tunnel förekommer det både vatten och luft i sprickorna. Luften ansamlas i de vidaste delarna av sprickorna på grund av kapilärtrycket vilket leder till att konduktiviteten minskar. Den effektiva konduktiviteten beroende av variansen på konduktiviteten och effekterna av utsläckning av högkonduktiva celler har också studerats. En diskussion rörande hur luft i sprickor kring en tunnel kan orsaka skineffekter genomförs och exempel ges på effekter som kan uppstå på grund av flödesberoende mättnadsgrad.

PREFACE

This report was originally published as a licentiate thesis: Groundwater flow through a natural fracture. Flow experiments and Numerical Modelling. Department of Geology, Chalmers University of Technology [Chalmers tekniska högskola, Geologiska institutionen, Publ. A 82, ISSN 1104-9839].

The work presented in this report was performed at the Department of Geology, Chalmers University of Technology, under the supervision of Professor Gunnar Gustafson.

I would like to express my sincere thanks to Professor Gunnar Gustafson for giving me the opportunity to start as Ph.D. student. Thank you for introducing me to the field of hydrogeology, for valuable guidance, suggestions and helpful discussions.

The financial supports from Swedish Nuclear Fuel and Waste Management Company (SKB) are gratefully acknowledged. Thanks to Dr. Lars O Ericsson for a dedicated interest for the project and for encouragement during the work.

Parts of the work have been done in cooperation with the Division of Engineering Geology at the Royal Institute of Technology (KTH) in Stockholm. Special thanks to Dr. Eva Hakami (nowadays Itasca geomekanik AB) for stimulating and fruitful collaboration. It has been a pleasure to work with you. My sincere gratitude also to Professor Ove Stephanson for support and discussions during the work.

I would also thank all friends and former colleagues at the Department of Geology for the friendly and stimulating atmosphere. Whether among fellow Ph.D. students, senior scientists or the technical/administrative staff I have always enjoyed your company. You are too numerous to be mentioned by name. Let me merely thank Chester, David, Lars and Per for correcting my English in this and other manuscripts.

Thanks also to my present colleagues at MDC for your patience with me during the time I have been working with this report.

Thanks to all other friends, always caring and giving me good times.

Finally, my special thanks to my wife: Thank you Anette for being there whenever I needed you!

Erik Larsson

- | | |
|--|---|
| <p>1 <i>"Surely there is a mine for silver, and a place for gold which they refine.</i></p> <p>2 <i>Iron is taken out of the earth, and copper is smelted from the ore.</i></p> <p>3 <i>Men put an end to darkness, and search out to the farthest bound the ore in gloom and deep darkness.</i></p> <p>4 <i>They open shafts in a valley away from where men live; they are forgotten by travelers, they hang afar from men, they swing to and fro.</i></p> <p>5 <i>As for the earth, out of it comes bread; but underneath it is turned up as by fire.</i></p> <p>6 <i>Its stones are the place of sapphires, and it has dust of gold.</i></p> <p>7 <i>"That path no bird of prey knows, and the falcon's eye has not seen it.</i></p> <p>8 <i>The proud beasts have not trodden it; the lion has not passed over it.</i></p> <p>9 <i>"Man puts his hand to the flinty rock, and overturns mountains by the roots.</i></p> <p>10 <i>He cuts out channels in the rocks, and his eye sees every precious thing.</i></p> <p>11 <i>He binds up the streams so that they do not trickle, and the thing that is hid he brings forth to light.</i></p> <p>12 <i>"But where shall wisdom be found? And where is the place of understanding?</i></p> <p>13 <i>Man does not know the way to it, and it is not found in the land of the living.</i></p> | <p>14 <i>The deep says, 'It is not in me,' and the sea says, 'It is not with me.'</i></p> <p>15 <i>It cannot be gotten for gold, and silver cannot be weighed as its price.</i></p> <p>16 <i>It cannot be valued in the gold of Ophir, in precious onyx or sapphire.</i></p> <p>17 <i>Gold and glass cannot equal it, nor can it be exchanged for jewels of fine gold.</i></p> <p>18 <i>No mention shall be made of coral or of crystal; the price of wisdom is above pearls.</i></p> <p>19 <i>The topaz of Ethiopia cannot compare with it, nor can it be valued in pure gold.</i></p> <p>20 <i>"Whence then comes wisdom? And where is the place of understanding?</i></p> <p>21 <i>It is hid from the eyes of all living, and concealed from the birds of the air.</i></p> <p>22 <i>Abaddon and Death say, 'We have heard a rumor of it with our ears.'</i></p> <p>23 <i>"God understands the way to it, and he knows its place.</i></p> <p>24 <i>For he looks to the ends of the earth, and sees everything under the heavens.</i></p> <p>25 <i>When he gave to the wind its weight, and meted out the waters by measure;</i></p> <p>26 <i>when he made a decree for the rain, and a way for the lightning of the thunder;</i></p> <p>27 <i>then he saw it and declared it; he established it, and searched it out.</i></p> <p>28 <i>And he said to man, 'Behold, the fear of the Lord, that is wisdom; and to depart from evil is understanding.'"</i></p> |
|--|---|

Job 28. (Scripture taken from the Revised Standard Version.)

TABLE OF CONTENTS

	ABSTRACT (ENGLISH)	i
	ABSTRACT (SWEDISH)	iii
	PREFACE	v
	TABLE OF CONTENTS	vii
	LIST OF SYMBOLS	ix
1	INTRODUCTION	1
2	GROUNDWATER FLOW IN FRACTURED ROCK	3
2.1	FLOW IN A SINGLE FRACTURE	3
2.2	FLOW IN FRACTURE SYSTEMS	6
3	NUMERICAL MODELS OF FRACTURE FLOW	7
3.1	MODELLING APPROACHES	7
3.1.1	Discrete fracture network, DFN	8
3.1.2	Stochastic continuum, SC	8
3.1.3	Channel network models, CN	8
3.2	FDM-MODELLING	9
3.2.1	Conductance between the cells	10
3.2.2	Comparison between the cases	13
3.2.3	The effective conductivity dependence of the variance	14
3.2.4	Effects of the boundaries	15
4	MODELLING BASED ON PUBLISHED DATA OF FRACTURE APERTURE	19
4.1	MODELLING OF FLOW	19
4.2	MODELLING OF TRANSPORT	22
5	FLOW EXPERIMENTS IN A NATURAL FRACTURE	25
5.1	FRACTURE SAMPLE	25
5.1.1	Sampling technique	25
5.1.2	Description of the sample	25
5.2	EXPERIMENTAL SETUP	26
5.2.1	Biaxial cell	26
5.2.2	Water flow arrangements	28
5.2.3	Pressure measuring points	29
5.2.4	Displacement gauges	30

5.3	EXPERIMENTAL RESULTS	30
5.3.1	Flow, transmissivity and hydraulic aperture	30
5.3.2	Compressibility and storage coefficient	32
5.3.3	Tracer test	35
5.3.4	Pressure measuring points	37
6	FRACTURE APERTURES	39
6.1	GROUTING WITH EPOXY RESIN	39
6.2	APERTURE MEASUREMENTS	40
7	MODELLING OF THE FLOW EXPERIMENTS	45
7.1	FDM-MODELING OF THE FLOW	45
7.2	TRACER SIMULATION	48
7.3	ESTIMATION OF THE FLOW BASED ON THE APERTURE MEASUREMENTS	49
8	SOME NOTES ON TWO-PHASE FLOW IN FRACTURES	51
8.1	THE PRINCIPLES OF TWO-PHASE FLOW	51
8.2	THE EFFECT OF EXTINCTION OF HIGHLY CONDUCTIVE CELLS	55
8.3	SKIN EFFECT CAUSED BY GAS LIBERATION	57
8.4	EFFECTS OF FLOW-DEPENDING SATURATION	59
9	CONCLUSIONS	61
	REFERENCES	63
	APPENDIXES	
	Appendix 1 Description of Geoblock	
	Appendix 2 Measured data	
	Appendix 3 Technical specification of Epofix	

LIST OF SYMBOLS**LATIN LETTERS**

b	aperture	[L]
b_1, b_2	aperture one and two respectively	[L]
b_G	geometric mean of aperture	[L]
B	random variable with a normal distribution $N(0,1)$	[-]
c	contact area extent	[-]
C	integration constant in Chapter 3.2.1	[L]
C	concentration	[ML ⁻³]
C_0	initial concentration	[ML ⁻³]
$D(u)$	function defined in Equation (32)	[-]
e	hydraulic aperture	[L]
\tilde{f}_n	Fourier coefficients	[L]
F	ratio of water to oil viscosity	[-]
g	gravity acceleration	[L ¹ T ⁻²]
G	constant in Equation (9)	[-]
h	water pressure head	[L]
h_0	water pressure head at the upper end of the sample	[L]
h_1, h_2	water pressure head in the center of cell one and two, respectively	[L]
h_{12}	water pressure head at the boundary between cell one and two	[L]
i	gradient	[-]

I_p	productivity index	[-]
k	permeability	[L ²]
k_r	relative permeability	[-]
k_{ro}, k_{rw}	relative permeability for oil and water, respectively	[-]
K	hydraulic conductivity	[LT ⁻¹]
K_0	hydraulic conductivity at total saturation	[LT ⁻¹]
K_{eff}	effective hydraulic conductivity	[LT ⁻¹]
K_1, K_2	hydraulic conductivity in the center of cell one and two, respectively	[LT ⁻¹]
K_{12}	hydraulic conductivity at the boundary between cell one and two	[LT ⁻¹]
K_G	geometric mean of hydraulic conductivity	[LT ⁻¹]
L	length of sample	[L]
P	pressure	[FL ⁻²]
P_c	capillary pressure	[FL ⁻²]
q	flow rate	[LT ⁻¹]
Q	volumetric flow rate	[L ³ T ⁻¹]
Q_c	volumetric flow rate calculated with the cubic law used on the average of the aperture	[L ³ T ⁻¹]
Q_m	measured volumetric flow rate	[L ³ T ⁻¹]
Q_v	volumetric flow rate calculated from velocity measurements	[L ³ T ⁻¹]
$Q_{\text{without skin}}$	volumetric flow rate if no skin effect had occur	[L ³ T ⁻¹]
$Q_{\text{with skin}}$	volumetric flow rate reduced owing to skin effect	[L ³ T ⁻¹]
r	radius	[L]
r_2	radius of zone with reduced conductivity	[L]

r_w	radius of the tunnel in Chapter 8.3	[L]
Re	Reynolds number	[-]
R_0	radius of influence	[L]
S	storage coefficient	[-]
S	saturation	[-]
S_m	saturation of the non-wetting phase at which it is reduced to unconnected bubbles	[-]
S_{or}, S_{wr}	irreducible saturation for oil and water, respectively	[-]
S_r	irreducible saturation of wetting phase	[-]
s	drawdown	[L]
s_g	difference in water table head defined in Chapter 8.3	[L]
s_w	drawdown of the water table head at the tunnel wall in Chapter 8.3	[L]
t	time	[T]
T	transmissivity	[L ² T ⁻¹]
u	$\frac{SL^2}{Tt}$ used as dimensionless parameter	[-]
v	mean velocity	[LT ⁻¹]
W	width of the sample	[L]
x	coordinate at right angle to the sample	[L]
y	coordinate at right angle to the fracture	[L]
z	coordinate parallel with the sample	[L]

GREEK LETTERS

α	proportional constant in Chapter 3.2.1	[-]
α_L	longitudinal intrinsic dispersion coefficient	[L]

β	expresses the ratio of the magnitude of viscous to capillary forces	[-]
γ	angle	[°]
δ	reducing factor of the conductivity around a tunnel	[-]
Δh	difference of water pressure head	[L]
Δx	length of a cell in x direction	[L]
ζ	relate the saturation to the flow, Chapter 8.4	[TL ⁻³]
θ	contact angle	[°]
θ_A	advancing contact angle	[°]
θ_R	receding contact angle	[°]
θ	moisture content	[-]
κ	compressibility	[L ² F ⁻¹]
κ_w	compressibility of water	[L ² F ⁻¹]
μ	mean of the logarithm of the conductivity	[ln (LT ⁻¹)]
μ	dynamic viscosity	[ML ⁻¹ T ⁻¹]
μ_o, μ_w	dynamic viscosity for oil and water, respectively	[ML ⁻¹ T ⁻¹]
ξ	skin factor	[-]
Π	pressure distribution	[FL ⁻²]
ρ	density	[ML ⁻³]
σ	standard deviation of the logarithm of the conductivity	[-]
σ^2	variance of the logarithm of the conductivity	[-]
σ_b	standard deviation of the aperture	[-]
χ	group of variables that describe the roughness	[-]
Ψ	distribution of water pressure head	[L]
Ψ_0	difference of water pressure head	[L]

ω total porosity [-]

USED STATISTICAL SYMBOLS

$\text{cov}[a,b]$ the covariances of the two random functions a and b .

$E[a]$ expected value of the random function a .

$N(\mu,\sigma)$ normal distribution with the mean μ and a standard deviation σ .

INTRODUCTION

Groundwater flow and transport play an important role not only for groundwater exploration but also in environmental engineering problems. In crystalline rock the flow is controlled by the fracture network and its hydraulic properties. In turn, this depends on the properties of the single fractures. To predict the flow in a fracture, the knowledge of the following factors is required: the fluid property, the boundary conditions, and the fracture void geometry. This report considers how the hydraulic properties of fractures in crystalline rock depend on the fracture aperture geometry and the study can logically be subdivided into three parts.

Part I consists of Chapter 2 to Chapter 4. In this part we are discussing groundwater flow in fractured rock in general and various approaches of estimating the transmissivity. Different numerical models are presented and a couple of relations between the cells in a FDM-model are compared. In Chapter 4 this FDM-model is used to modelling the flow based on published data of aperture distributions.

Part II consists of Chapter 5 to 7. This part deals with the laboratory experimental work where flow experiments and aperture measurements on the same specimen of a natural fracture are carried out. This made it possible to make a direct comparison between calculations and experiments which is desirable.

The different parts of the laboratory work are illustrated in Figure 1-1. A core was drilled with a fracture parallel with the length axis of the core. The core was held under compression with a biaxial cell, a constant water pressure was applied to the lower end of the core and the flow was recorded from the overflow at the top. After that the flow measurements were finished the fracture was injected with fluorescent epoxy while it still was in the biaxial cell. After that the epoxy had hardened the core was cut up in profiles and these profiles were examined with a microscope connected to an image analysis system. Using the obtained aperture distribution, a statistical analysis and aperture simulations were carried out to calculate the flow. Chapter 5 considers the flow measuring part, Chapter 6 is dealing with the aperture measurements which were done by Eva Hakami, Royal Institute of Technology, and Chapter 7 consider the aperture simulations and flow calculations. Also the appendices belong to part II.

Part III consists of Chapter 8 where we discuss the effects of two-phase flow. We noticed that in a fracture with varying aperture, the gas will go to the widest part of the fracture because of the capillarity. The most permeable

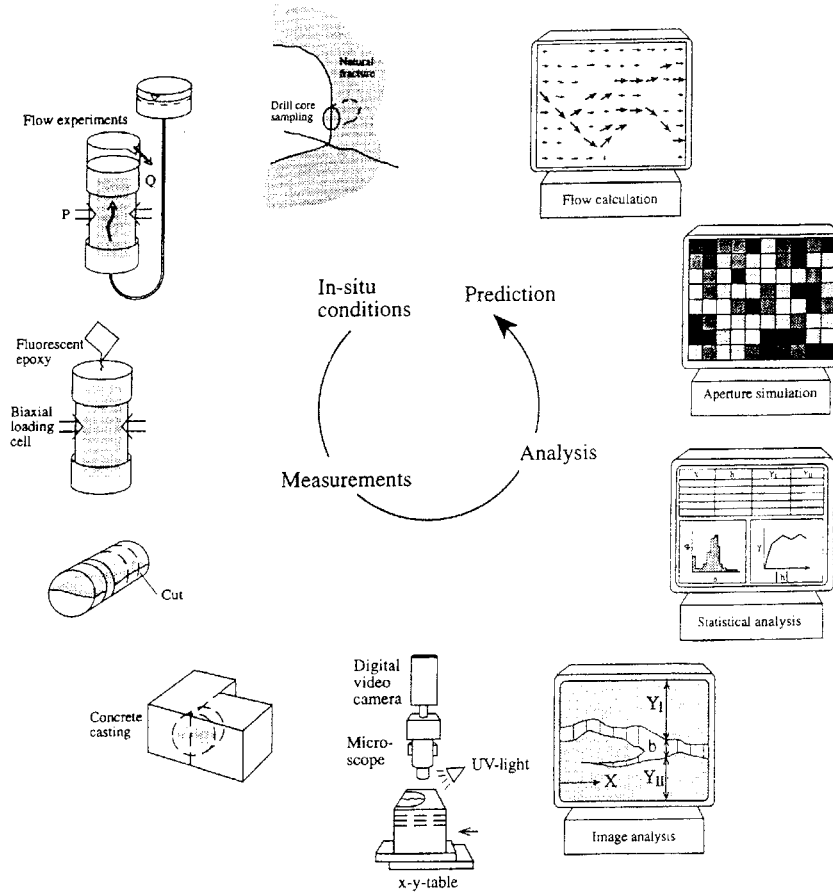


Figure 1-1. The different steps taken in the laboratory experimental work.

parts of the fracture are thus filled with air and can not conduct water, and the total permeability decreases. A study is done on the effect of extension of highly conductive parts on the effective conductivity. We are also discussing how gas in fractures around a drift can cause a skin effect which is modelled and an example is given of what a saturation depending on the magnitude of the flow causes.

GROUNDWATER FLOW IN FRACTURED ROCK

The groundwater flow in a rock can occur both in the rock matrix and in the fractures. What part which is dominating depends of the porosity and properties of the fractures. It is clear that for rock types with low porosity, the fracture flow is the most important, but also for highly permeable rock types, the fracture flow can be important. This is illustrated in Figure 2-1 /Maini and Hacking, 1977 /. For example, the flow through a 100-m-thick cross-section of a porous medium with a hydraulic conductivity of 10^{-7} m/s might also come from one single fracture with an opening not wider than 0.2 mm in a fractured medium with an impervious rock matrix.

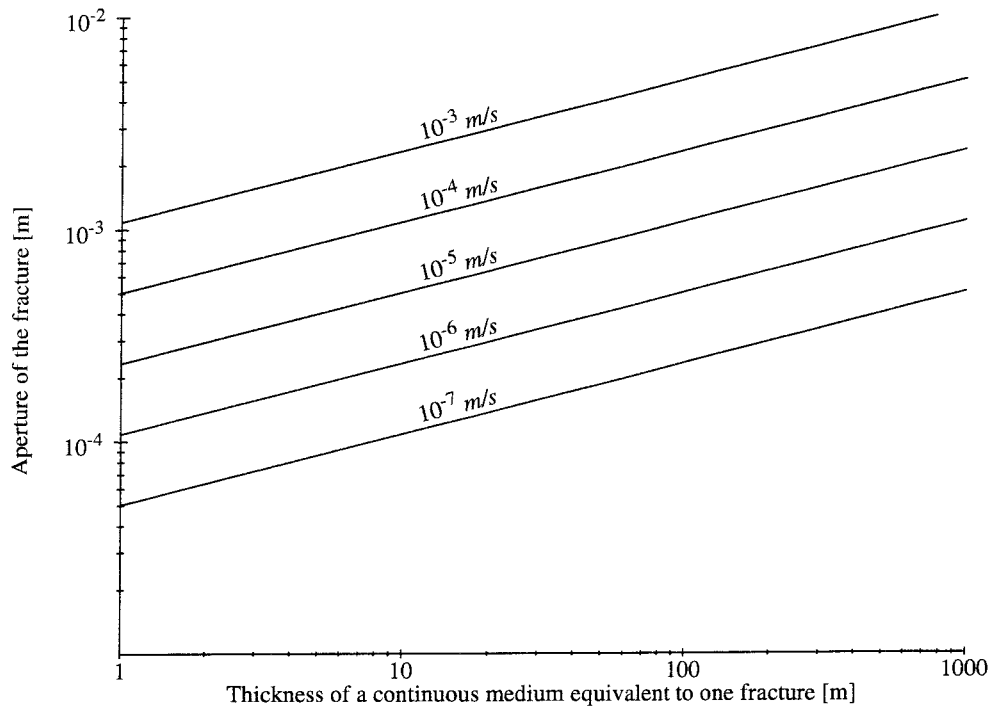


Figure 2-1. Comparison between the hydraulic conductivity of the porous medium and the fractured medium versus the aperture. After Maini and Hacking, /1977 /.

2.1

FLOW IN A SINGLE FRACTURE

For flow in porous media, Darcy's law can be used if the medium is homogeneous and isotropic and the representative element volume, REV, is small compared to the scale of the studied problem. It is not obvious that

these conditions are fulfilled in the case of a fractured rock. However, it can be shown that at a local scale there is an analogy between Darcy's law and the flow in a single fracture.

A laminar viscous flow between two parallel plates can be described with the cubic law:

$$Q = -\frac{\rho g W b^3}{\mu 12} i \quad (1)$$

where Q is the flow, ρ and μ are the density and viscosity of the fluid, respectively, g is the gravitational acceleration, i is the head gradient, W the width of the sample and b is the aperture, i.e. the distance between the two plates. The analogy with Darcy's law is clear which states:

$$Q = -WTi \quad (2)$$

where T is the transmissivity. The transmissivity of the fracture between the two plates can thus be written as

$$T = \frac{\rho g b^3}{\mu 12} \quad (3)$$

and the hydraulic conductivity, K , i.e. the transmissivity divided with the aperture

$$K = \frac{\rho g b^2}{\mu 12} \quad (4)$$

In reality fracture surfaces are neither smooth nor parallel. However, local parallelism can generally be accepted approximately true, which means that there is a conductivity distribution over the fracture plane which is related to the aperture distribution. In order to use the cubic law to predict transmissivity of a real rock fracture, one can assume that Equation (3) still holds if the aperture b is replaced by the mean aperture $E[b]$. Although replacing b with $E[b]$ is a first approximation to the actual transmissivity, the effects of roughness and obstructions are not properly accounted /Zimmerman and Bodvarsson, 1996 /. This suggests that we define the so-called hydraulic aperture e in terms of the actual transmissivity T :

$$T = \frac{\rho g e^3}{\mu 12} \quad (5)$$

The problem of relating the transmissivity of a fracture to its geometry can therefore be thought of in terms of finding an expression for the hydraulic aperture e .

The effective macroscopic transmissivity depends not only on the statistical distribution of the local transmissivities, but also on the geometrical and topological manner in which the local conductivity is distributed. Assume that we have a fracture in which the aperture varies either only in the direction of flow, or only in the direction transverse to the flow. It can then be shown /Dagan, 1979 / that the first case leads to $e^3 = 1/E [1/b^3]$, which is a lower bound to the actual isotropic transmissivity. The second case leads to $e^3 = E [b^3]$, which is an upper bound to the actual isotropic transmissivity. The two boundaries are thus the harmonic mean and the arithmetic mean, respectively.

In the case of a statistically isotropic two-dimensional medium with log-normal distributed conductivities, Gutjahr et. al. /1978 / have shown that

$$K_{eff} = K_G \quad (6)$$

where K_G is the geometric mean defined by $\ln K_G = E[\ln K]$. This result can also be expressed in terms of hydraulic aperture /Zimmerman & Bodvarsson, 1996 /

$$e^3 \approx E [b]^3 (1 - 1.5\sigma_b^2/E [b]^2 + \dots) \quad (7)$$

where σ_b is the standard deviation of the aperture. Also the geometric mean of b can be used to estimate e /Piggott and Elsworth, 1993 /

$$e^3 = b_G^3 \quad (8)$$

This estimation is accurate for log-normal aperture distributions, but it is not obvious that Equation (8) is preferable to Equation (7) in the general case.

Several other attempts to incorporate fracture roughness in the expression of hydraulic conductivity have been done. Most of them are of the form

$$K = \frac{\rho g}{\mu} \frac{b^2}{12 [1 + G (\chi)^n]} \quad (9)$$

where G is some constant larger than one, χ is a group of variables that describe the roughness, and n is some power greater than one /Domenico and Schwartz, 1990 /. Hence, roughness causes a decrease in hydraulic conductivity.

The state of stress in the rock mass will not influence the conductivity directly, but a change in stress will change the fracture geometry, and therefore also the groundwater flow. This is important to remember for

experiments of fracture flow. Both for laboratory experiments when an external pressure has to be applied, and for in situ experiments, when the stress field can be influenced by the experiment.

Kirkpatrick /1973 / has shown the effect of contact areas. Assume that we divide our fracture plane in squares and let each square have either aperture b with probability $(1-c)$, or aperture 0 with probability c , the cube of the hydraulic aperture will become

$$e^3 = b^3 (1 - 2c) \quad (10)$$

This equation also predict the existence of a percolation limit, which is the value of the contact area ($c = 0.5$) at which the flow is completely obstructed. Although it seems reasonable that a sufficiently large amount of contact area will block off all flow paths, contact areas as large as 0.5 have not been reported very often in the literature, so for practical purposes this issue may be irrelevant. Nevertheless, the fact that Equation (10) incorporates the percolation phenomena in some manner is an additional argument for its use in estimating the tortuosity /Zimmerman, 1996 /.

2.2

FLOW IN FRACTURE SYSTEMS

Fractures can generally be divided into several fracture sets with different geological history, orientations and properties. The different fracture sets will build up a network of fractures, more or less interconnected. The flow in this fracture system will not only depend on the hydraulic conductivity of the individual fractures. It will also depend on the orientation, size, fracture density, and degree of connectivity of the fractures. Different approaches of calculation of the flow in fracture systems are discussed in Section 3.1.

3.1 MODELLING APPROACHES

At the local scale, the hydraulic properties in fractured rock are heterogeneous. To simulate this heterogeneity different modelling approaches are used. The three most common approaches are illustrated in Figure 3-1 from Geier et al. /1992 /. Each type of model has particular advantages and disadvantages for modelling of fractured rock masses.

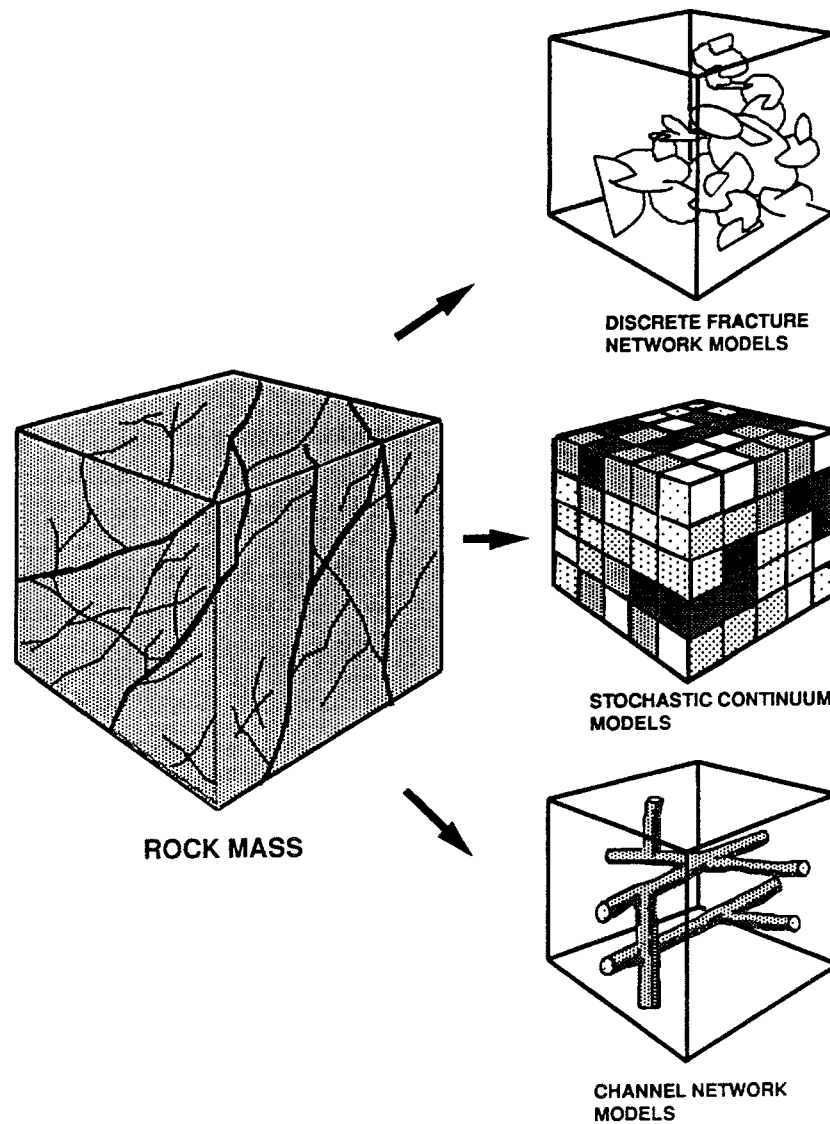


Figure 3-1. Different modelling approaches. After Geier et al. /1992 /.

3.1.1 **Discrete fracture network, DFN**

A discrete fracture network (DFN) model is built up from a statistical description of fracture geometry and hydraulic properties such as the location, size, orientation, spatial structure, transmissivity and intensity. The flow paths are assumed to result from networks of interconnecting fractures. The most important advantage of the DFN model are the possibility to incorporate fracture geometry data in the model and explicitly represent properties of fractures and fracture zones. On the other hand, fracture data over the total region that would be modelled is required. Therefore, it might be necessary to simplify the fracture pattern, both because of the complexity of the network and because fracture data are unknown.

3.1.2 **Stochastic continuum, SC**

The stochastic continuum (SC) approach is based on the idea that a formation can be described in terms of physical parameters that vary in space according to spatially random functions. The modelled region is divided into cells and each cell is given certain properties based on the random functions. Using a finite element model or a finite difference model, the global properties can be calculated. The SC approach results in models, which are based on extensive well-known theory and are easy to realize. A major question is if it is suitable with a continuum approach in a fractured rock model or not. Usually it is assumed that on some averaging scale, a porous medium behavior with an effective hydraulic conductivity, K , exists which forms a continuous random field. However, this assumption may not be valid for all scales. It is also possible to use a SC model on the scale of a single fracture, which will be performed later in this report.

3.1.3 **Channel network models, CN**

The concept of a channel network (CN) model is that the flow within a fracture network is confined to discrete channels, which intersect at various intervals. Like the DFN model, CN models are based on the discrete nature of the fracture pathways. Using a network composed of effectively one-dimensional elements the computational difficulty can be reduced and, thus, this approach simplifies the modelling of complex processes. The data requirements for a CN model are also somewhat less than for a DFN model, because the characteristics of fracture geometry are ignored. A problem is the validation of the assumptions about channel geometry, that are needed to appraise the channel frequencies and length distribution. Another problem is that a change in direction of the gradient may change the channel pattern which means that each channel network should be constructed for a certain flow direction.

3.2 FDM-MODELLING

Using the Geoblock computer code (see Appendix 1), developed at the Department of Geology at Chalmers University of Technology, a three-dimensional flow-modelling was performed to study the dependence of effective conductivity on the distribution of the conductivity. Geoblock is based upon the spreadsheet code Wingz¹ and is primarily intended for flow-modelling in three dimensions with heterogenous conductivities. The code is very general and is useful for all potential- and flow-problems which can be handled as a stochastic continuum (Chapter 3.1.2) in two or three dimensions.

The used models are blocks over which a one-dimensional pressure gradient was applied. We thus got a three-dimensional flow through the model with a main flow direction. The standard size of the blocks in the simulations was $20 \times 20 \times 20$ cells. We have found, in comparison with other sizes, that we can use this size of models without any problems regarding the boundaries. According to several studies, the hydraulic conductivity can be described using a log-normal distribution /Freeze 1975, Bakr et al. 1978, Gustafson and Åberg 1985, among others /.

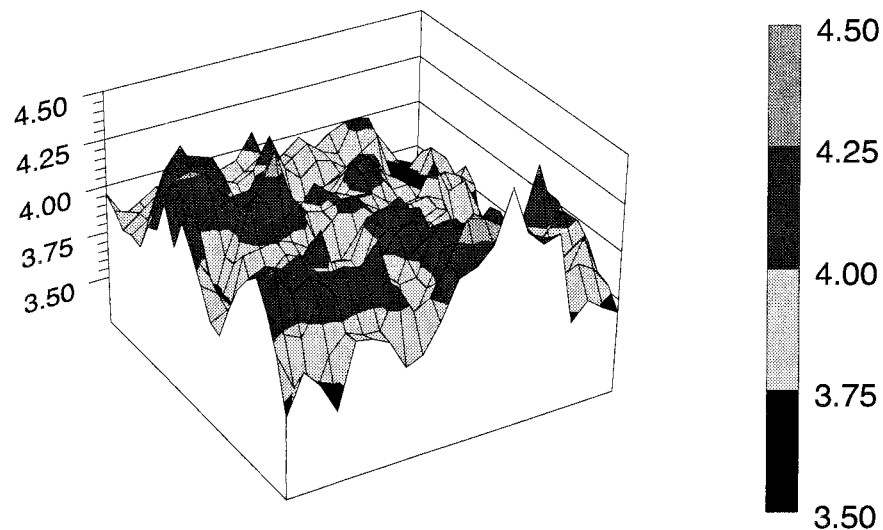


Figure 3-2. Example of the pressure distribution over a cross-section at a right angle to the principal direction of flow in a 3D-model with a log-normally distributed conductivity.

The cells in the models were given a log-normally distributed conductivity, which for the separate cells was calculated as

1. Wingz is a trademark of Informix Software, Inc. 160 11 College Boulevard, Lenexa, Kansas 66219.

$$K = e^{B\sigma + \mu} \quad (11)$$

where B is a random variable with a normal distribution $N(0, 1)$. This gives $\ln K$ a normal distribution $N(\mu, \sigma)$, where μ is the mean and σ is the standard deviation.

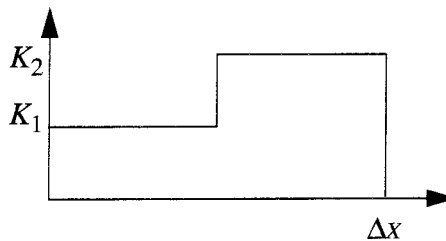
3.2.1 Conductance between the cells

The conductance between the cells can be calculated in different ways, according to different assumptions of how the conductivity varies between the cells. Five different cases were studied, which all gave different results.

3.2.1.1 Discrete variation

In this case, and also in the following cases we will use a notation where K_1 and K_2 are the conductivity in the center of the two cells which we calculate the flow between. h_1 and h_2 are the heads in the center of the cells and h_{12} is the head at the cell boundaries. The length between the centers is Δx and q is the flow between the cells divided with the cross area of the cells.

In this first case we have the ordinary case where the conductivity is constant in every cell and changes at the border of the cell. This is the case which was used originally in Geoblock.



$$q = -\frac{dh}{dx}K = \frac{h_1 - h_{12}}{\frac{\Delta x}{2}}K_1 = \frac{h_{12} - h_2}{\frac{\Delta x}{2}}K_2$$

$$h_{12} = \frac{h_1 K_1 + h_2 K_2}{K_1 + K_2}$$

$$q = \frac{2}{\Delta x} \left[\frac{h_1 K_1 + h_2 K_2}{K_1 + K_2} - h_2 \right] K_2 = \frac{2}{\Delta x} \left[\frac{h_1 K_1 - h_2 K_1}{K_1 + K_2} \right] K_2 = \frac{h_1 - h_2}{\Delta x} \frac{2K_1 K_2}{K_1 + K_2}$$

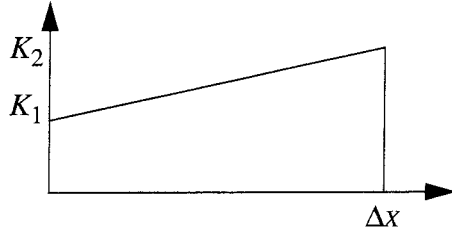
This gives us a relative conductivity, which can be written as

$$K_{12} = \frac{2K_1 K_2}{K_1 + K_2} \quad (12)$$

which is the harmonic mean of K_1 and K_2 .

3.2.1.2 Linear variation

In this case there is a linear variation of the conductivity between the cells. The conductivity is not so closely connected to the cells in this case as in the discrete case, because there is no step of the conductivity at the borders of the cells.



$$K = K_1 + \alpha x \quad ; \quad dK = \alpha dx$$

$$K_2 = K_1 + \alpha \Delta x \quad ; \quad \alpha = \frac{K_2 - K_1}{\Delta x}$$

$$q = -\frac{dh}{dx}K \quad ; \quad -dh = q \frac{dx}{K} = \frac{q dK}{\alpha K} \Rightarrow -h = \frac{q}{\alpha} \ln K + C$$

$$\begin{aligned} \Delta h = h_2 - h_1 &= \frac{q}{\alpha} (\ln K_1 - \ln K_2) = q \Delta x \frac{\ln (K_1/K_2)}{K_2 - K_1} \Rightarrow \\ &\Rightarrow q = -\frac{\Delta h}{\Delta x} \frac{K_2 - K_1}{\ln (K_2/K_1)} \end{aligned}$$

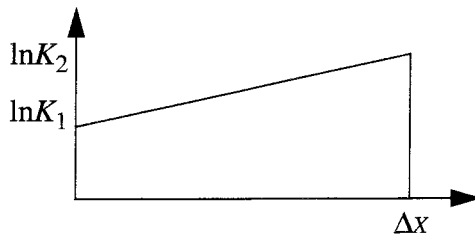
The relative conductivity is in this case

$$K_{12} = \frac{K_2 - K_1}{\ln (K_2/K_1)} \quad (13)$$

This equation can not be used if one of the conductivities is equal to zero, or if the transmissivity is uniform, but these cases can easily be handled separately.

3.2.1.3 Linear variation of the logarithm of the conductivity

In this case we have a variation which is linear with respect to the logarithm of the conductivity. This can be a reasonable assumption with respect to that the conductivity is log-normally distributed.



$$\ln K = \ln K_1 + \alpha x$$

$$K = K_1 e^{\alpha x} \quad ; \quad dK = \alpha K dx$$

$$\ln K_2 = \ln K_1 + \alpha \Delta x \quad ; \quad \alpha = \frac{\ln K_2/K_1}{\Delta x}$$

$$q = -\frac{dh}{dx}K \quad ; \quad -dh = q \frac{dx}{K} = \frac{q dK}{\alpha K^2} \Rightarrow -h = -\frac{q}{\alpha K} + C$$

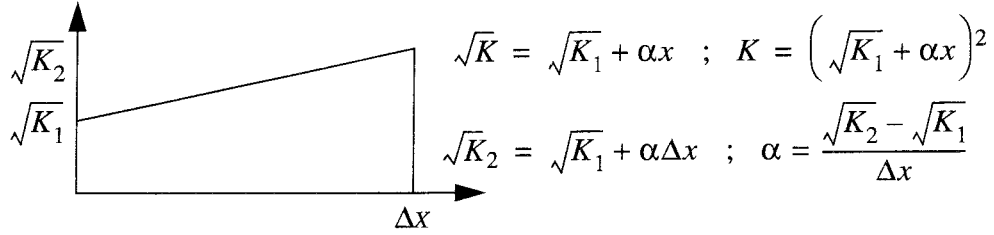
$$\Delta h = \frac{q}{\alpha} \left(\frac{1}{K_2} - \frac{1}{K_1} \right) = q \frac{\Delta x}{\ln (K_2/K_1)} \frac{K_1 - K_2}{K_1 K_2} \Rightarrow q = -\frac{\Delta h K_1 K_2 \ln (K_2/K_1)}{\Delta x (K_2 - K_1)}$$

And we get a relative conductivity

$$K_{12} = \frac{K_1 K_2}{K_2 - K_1} \ln (K_2 / K_1) \quad (14)$$

3.2.1.4 Linear variation of the square root of the conductivity

In this case we have a linear variation of the square root of the conductivity between the cells.



$$q = -\frac{dh}{dx}K ; -dh = q \frac{dx}{K} = \frac{q dx}{(\sqrt{K_1} + \alpha x)^2} \Rightarrow$$

$$\Rightarrow -h = \frac{-q}{\alpha(\sqrt{K_1} + \alpha x)} + C = -\frac{q}{\alpha \sqrt{K}} + C$$

$$\Delta h = \frac{q}{\alpha} \left(\frac{1}{\sqrt{K_2}} - \frac{1}{\sqrt{K_1}} \right) = \frac{q \Delta x}{\sqrt{K_2} - \sqrt{K_1}} \frac{\sqrt{K_1} - \sqrt{K_2}}{\sqrt{K_1 K_2}} \Rightarrow q = -\frac{\Delta h}{\Delta x} \sqrt{K_1 K_2}$$

which gives the relative conductivity

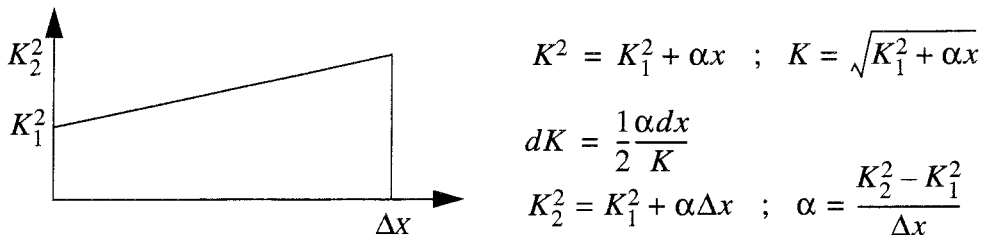
$$K_{12} = \sqrt{K_1 K_2} \quad (15)$$

This is the same as the geometric mean of K_1 and K_2 .

The geometric mean of the conductivities is however the theoretical solution of the effective conductivity for a two-dimensional flow /Gutjahr et al. 1978 / . Thus, this case might be important to study.

3.2.1.5 Linear variation of the squares of the conductivity

In this case there is a linear variation of the square of the conductivity in connection between both cells.



$$q = -\frac{dh}{dx}K \quad ; \quad -dh = q\frac{dx}{K} = \frac{2q}{\alpha}dK \Rightarrow -h = \frac{2q}{\alpha}K + C$$

$$\Delta h = \frac{2q}{\alpha}(K_1 - K_2) = 2q\Delta x \frac{K_1 - K_2}{K_2^2 - K_1^2} = \frac{-2q\Delta x}{K_1 + K_2} \Rightarrow q = -\frac{\Delta h}{\Delta x} \frac{K_1 + K_2}{2}$$

This time we get a relative conductivity, which is the same as the arithmetic mean.

$$K_{12} = \frac{K_1 + K_2}{2} \quad (16)$$

This is the trivial way to calculate a relative conductivity, but as we have seen it is not obvious to use just this case.

3.2.2 Comparison between the cases

If we compare the relative conductivities in the five different models, against the ratio between the conductivities in the two cells, we can see that they are all equal when the ratio is one and that they differ for all other values. The relative conductivity is smallest for the discrete case and larger for linear variations with respect to $\ln K$, \sqrt{K} , K and K^2 , respectively (Figure 3-3). We can also see that the divergence between the different cases increases with the ratio between the conductivities in both cells. The selection of type of connection thus has a greater impact as the variance of the conductivity increases.

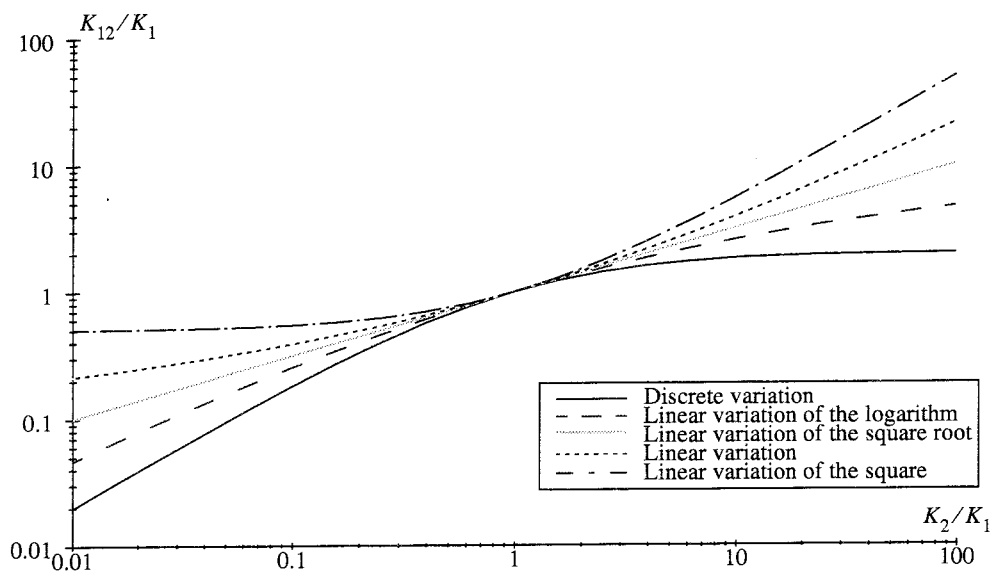


Figure 3-3. The relationship between K_2/K_1 and K_{12}/K_1 with the relative conductivity K_{12} calculated in five different ways.

3.2.3 The effective conductivity dependence of the variance

To study how the variance of the conductivity in the cells influences the effective bulk conductivity, the geometric mean of the conductivity in the cells, e^μ , was kept constant as the standard deviation, σ , was varied.

The effective conductivity increases with increased standard deviation, except for the discrete case, where it first decreases a little before it starts to increase (Figure 3-4). This is in agreement with Svensson /1992 /. The model used by Svensson is almost identical to our discrete case. On the other hand the discrete case does not correspond to the theoretical results by Gutjahr et al. /1978 /. They found that the effective conductivity for a three-dimensional flow can be described as

$$K_{eff} = e^\mu (1 + \sigma^2/6) \quad (17)$$

Gutjahr et al. used a proximal analytical solution based on a stochastic analysis, where the effective conductivity is calculated for a three-dimensional flow with a principal direction.

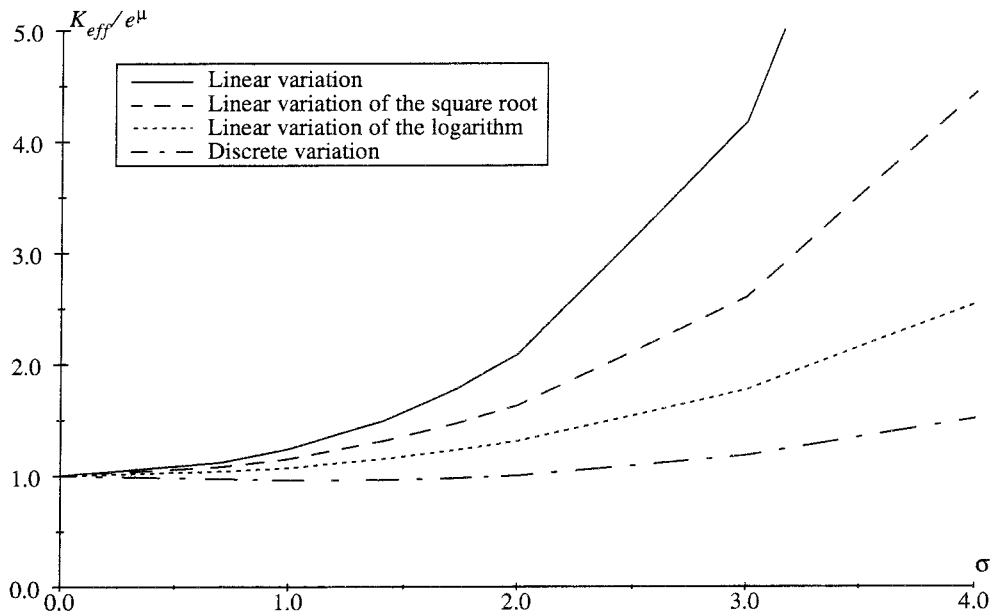


Figure 3-4. The effective conductivity as a function of the standard deviation σ .

According to Equation (17) a linear connection between the effective conductivity and the variance, σ^2 , of the logarithm of the conductivities in the cells is expected, i.e. the case with a linear variation of \sqrt{K} (Figure 3-5).

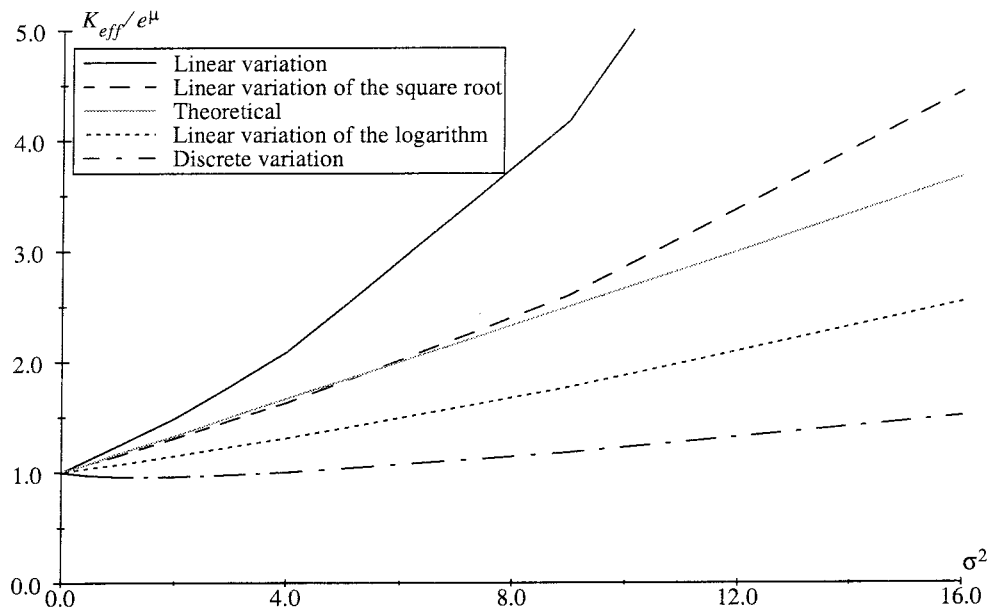


Figure 3-5. The effective conductivity as a function of the variance σ^2 .

One of the most probable reasons why a linear variation of \sqrt{K} is the best case regarding to the theory is that the flow between two cells is two- rather than three-dimensional and the relative conductivity we calculate in this case is the geometric mean of conductivities in the two cells, which is the theoretical solution of the effective conductivity for a two-dimensional flow.

3.2.4 Effects of the boundaries

If we make a cross-section in our model perpendicular to the principal direction of the flow, we can see how the flow will be distributed over the section. It appears that the location of the section in the model is important. The variance of the flow is greater close to the border of the model than at a section through the center of the model (Figure 3-6).

This means that the flow is more canalized close to a wall than inside the rock. This phenomenon can be related to the observation that the outflow in a tunnel occurs at fewer points than can be expected on basis of how much water can be extracted from a borehole. A simple way to explain this in our model is that the flow between two cells in the model depends on the pressure difference between the cells, which in turn influence each other. At the wall, the pressure in one of the cells is fixed so that a readjustment can not occur to the same extent.

However, independently of where the cross-section is taken in our model, the variance of the flow is always lower than the variance of the logarithm of the conductivities (Figure 3-7). We can also see that from the slope of the curves

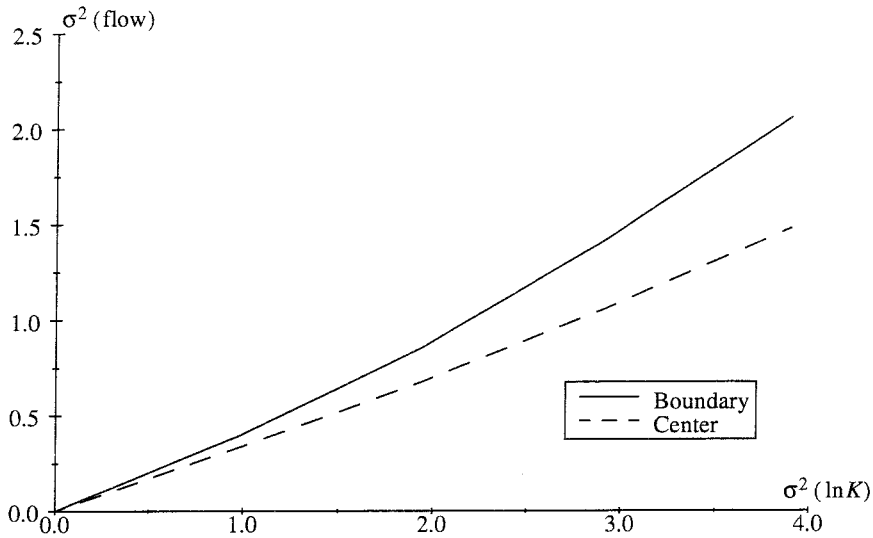


Figure 3-6. The variance of the flow as a function of the variance of the logarithm of the conductivities for a cross-section at the border of the model and at the center of the model.

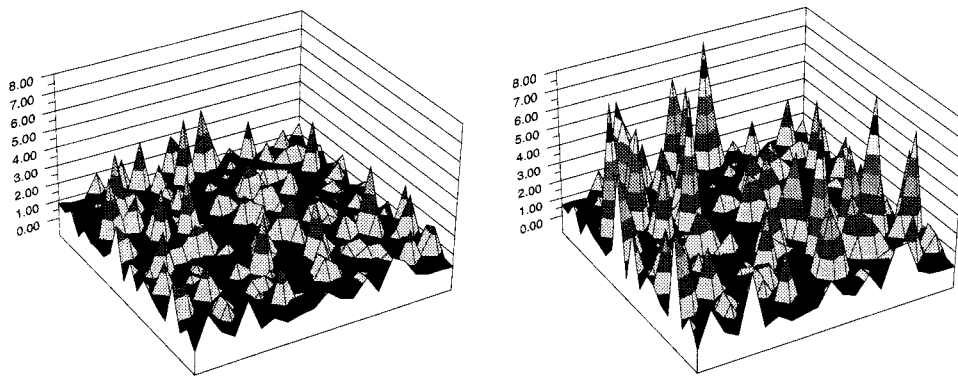


Figure 3-7. Examples of flow distribution and conductivity distribution in a cross-section at right angles to the principal direction of the flow. The section is situated at the center of the block.

in Figure 3-6. The flow is thus smoother than the conductivity field, which can be explained by the fact that the flow does not depend on the conductivity at one single point.

Because the flow is the product of the gradient and the conductivity, the gradient field must be smoother than both the flow and the conductivity field. It means that we have a negative correlation between the conductivity and the gradient field. This is important because we can calculate the expected value of the flow rate as:

$$E[q] = E[Ki] = E[K]E[i] + \text{cov}[K, i] \quad (18)$$

where $\text{cov}[K, i]$ is the covariance of the conductivity and the gradient, i . Since the covariance is negative, the expected value of the flow is smaller than the product of the expected values for the conductivity and for the gradient.

MODELLING BASED ON PUBLISHED DATA OF FRACTURE APERTURE

In 1988 Eva Hakami published her licentiate thesis. Hakami /1988 / showed results regarding aperture distribution measurements and water flow tests on five samples of single rock joints. To study the hydromechanical properties Hakami developed a technique to make transparent replicas of natural joint surfaces. The aperture distribution of the joints was obtained through a measurement method provided by the transparent replicas. The principle behind the method was that a water drop with a known volume, which is placed inside a joint, will cover a certain area of the surface depending on the size of aperture at the actual point. Also water flow tests were performed using the joint replicas. The tortuosity of the flow and the velocity along single stream lines were measured using color injections into the water flow through the joints.

4.1 MODELLING OF FLOW

Using Hakamis data of aperture measurements provided the opportunity to use real data in the FDM-model in order to compare the calculated flow with the measured flow. In that way the authenticity of the model could be tested.

In the model the transmissivity values are needed in a regular grid parallel to the orientation of the sample. Because of the fact that Hakamis measurement points were placed in a rotated grid (Figure 4-1), an estimation of the aperture in the points on the regular grid was required. The estimation was done by simple kriging involving the four nearest points.

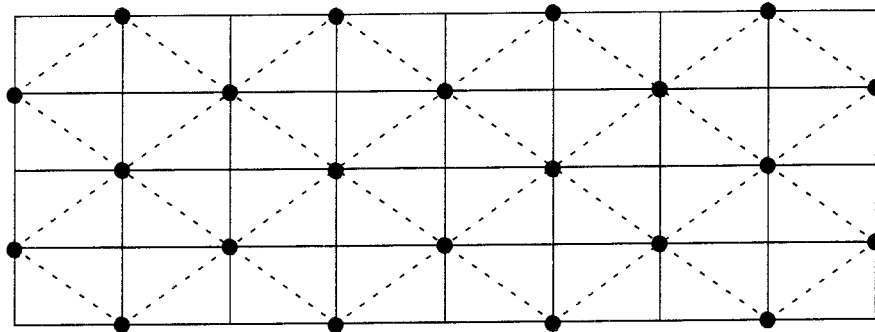


Figure 4-1. Schematic view of aperture measurement points position in a rotated grid according to the grid used in the FDM-model parallel to the sample.

The transmissivity T was then calculated in each point using the cubic law:

$$T = \frac{b^3 \rho g}{12\mu} \quad (19)$$

where b is the aperture, ρ and μ are the density and dynamic viscosity of water respectively and g is the gravity acceleration.

Using these transmissivity values in the FDM-model the water head distribution and the water flow was calculated. The results of the flow calculations are showed in Table 4-1 together with the measured flow and two different estimations of the flow by Hakami. The first estimation is calculated with the cubic law used on the average of the aperture for each sample and the second one is based on the velocity measurements.

Table 4-1. Compilation of measured, modelled and estimated flow per unit width. Q_m measured flow, Q modeled flow, Q_c estimated flow from cubic law, Q_v estimated flow from measured velocities.

Sample No.	Gradient $\Delta h/L$	$\frac{Q_m}{W} \left[\frac{\text{ml}}{\text{s m}} \right]$	$\frac{Q}{W} \left[\frac{\text{ml}}{\text{s m}} \right]$	$\frac{Q_c}{W} \left[\frac{\text{ml}}{\text{s m}} \right]$	$\frac{Q_v}{W} \left[\frac{\text{ml}}{\text{s m}} \right]$
B	0.32	3.48	2.40	7.76	1.69
	0.56	5.03	4.20	13.57	2.14
S2	0.14	9.03	7.70	12.10	4.77
	0.21	11.51	11.55	17.52	5.20
S3	0.31	2.22	7.81	23.80	0.95
	0.60	5.92	15.12	35.35	2.55
S4	0.18	1.43	2.34	2.67	1.30
	0.20	2.18	2.60	3.03	2.31
A2	0.70	1.28	1.17	2.46	0.87
	1.05	2.00	1.75	3.69	1.19

The modelled values are in the same order of magnitude as the measured ones except for sample S3. This is the sample where Hakami noticed the most unevenly distributed flow. About 80% of the flow result from three out of ten channels. It is also this sample which shows the largest ratio between the average mechanical aperture and the hydraulic aperture.

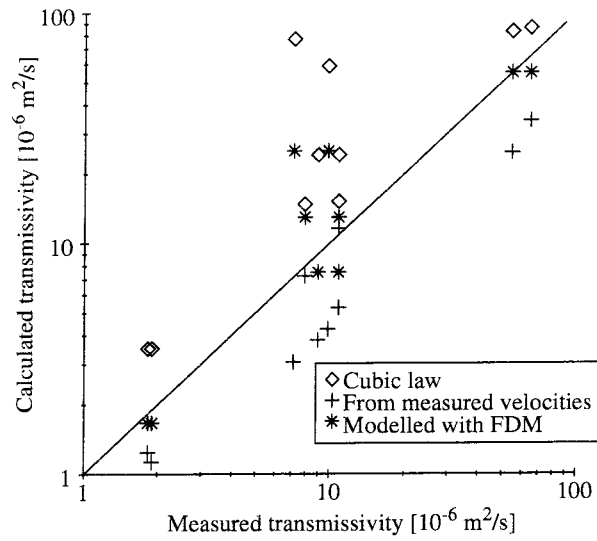


Figure 4-2. Measured effective transmissivity plotted against the modelled and estimated effective transmissivity.

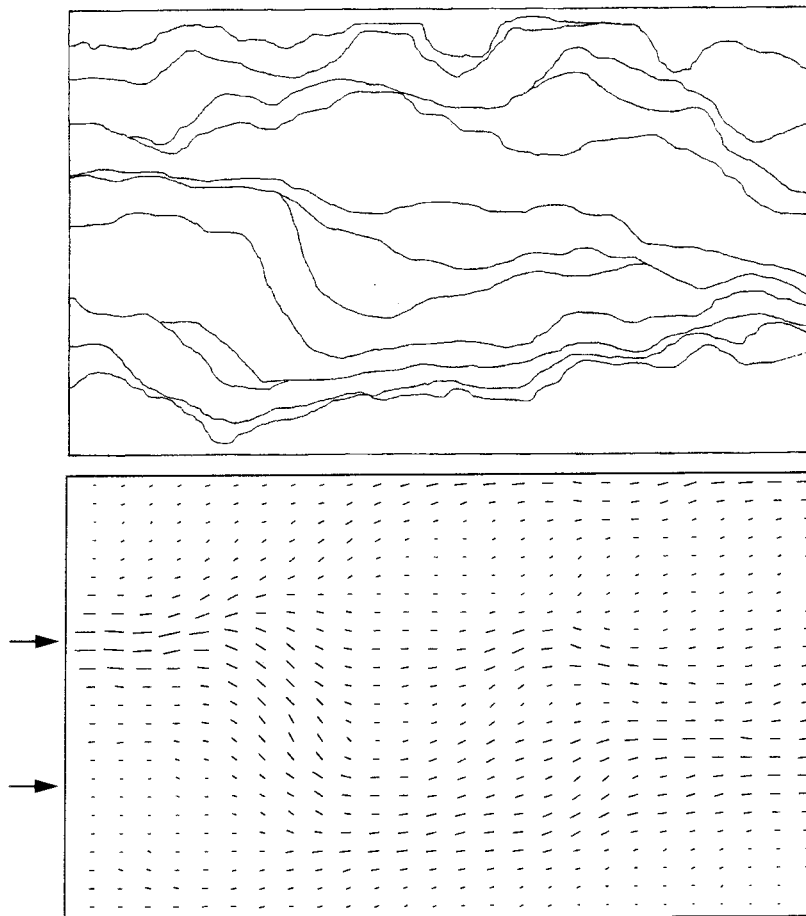


Figure 4-3. Illustration of flow tortuosity in a single fracture;
 a) Experimentally observed streamlines for sample S2, /Hakami, 1988 /;
 b) Calculated flow pattern for the same sample. The locations of the two injection cells in Figure 4-5 are also marked.

In Figure 4-2 are the measured effective transmissivity plotted against the modelled and estimated effective transmissivities. The modelled values are falling close to the one to one line while the estimated transmissivity values based upon the cubic law are overestimated and the estimations based on measured velocities are underestimated.

Using the head distribution it is also possible to visualize the flow tortuosity in the fracture. Figure 4-3a shows experimentally determined streamlines for sample S2 that has a large spread in the aperture distribution. Figure 4-3b shows the calculated flow pattern for the same sample.

4.2 MODELLING OF TRANSPORT

To simulate tracer experiments a particle tracking algorithm was used in the Geoblock code. The most probable flow path through the fracture was calculated by weighting the probability for each particle to go in a certain direction, with the percentage of the water volume which will go in that direction from the cell in which the particle resides for the moment.

Figure 4-4 is an example where the flow is coming from the left side of sample S2. One tracer particle was placed in each cell at the left side of the model to simulate a tracer experiment where the tracer was injected over the whole fracture side. It can be noticed that the particles follow the canalized flow shown in Figure 4-3. The time for first arrival with a gradient of 0.21 was 2.7 s which corresponds to a maximal transportation velocity of 0.04 m/s. The corresponding measured velocity for sample S2 was 0.05 m/s / Hakami 1988 /.

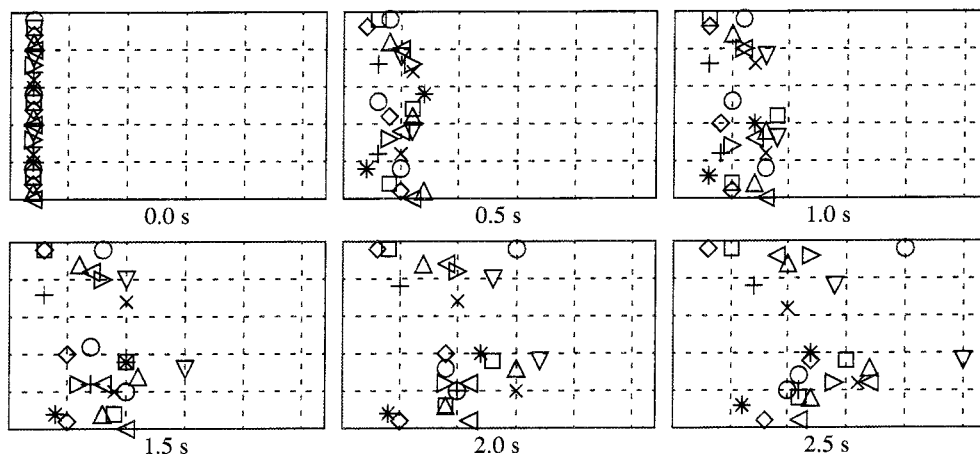


Figure 4-4. Different time steps in a simulated tracer experiment for sample S2. The tracer particles are injected over the whole side to the left of the fracture.

In Figure 4-5 the effect of dispersion in the model is shown. A number of particles were placed in two cells at the left side of the model. One of the two cells was placed in an area with locally high gradient and the other cell was placed in an area with locally low gradient. However, at the right the gradient field was different and even particles that started from the area with low gradient arrived first. The locations of the injections are also marked in Figure 4-3.

The particle in Figure 4-5 which is left behind in the area with low gradient illustrates a disadvantage of the used particle tracing algorithm. The flow in the model is divided in orthogonal components and if the main flow is almost parallel with the grid in the model the component perpendicular to the main flow will be small. However, a particle will have a small chance to go in the direction perpendicular to the main flow and it will take a long time before the particle arrives to next cell where it can go in the main direction again. This means that the dispersion can be greatly overestimated with the used algorithm.

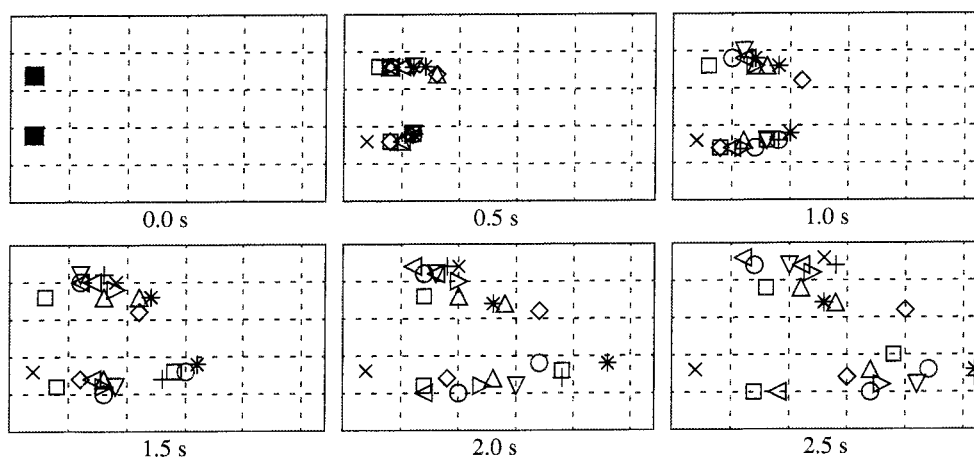


Figure 4-5. Simulated tracer experiment where the tracer particles are injected at two points at the side to the left of the fracture.

5 FLOW EXPERIMENTS IN A NATURAL FRACTURE

A flow experiment was performed on a drilled core with a fracture parallel with the length axis of the core. The core was held under compression with a biaxial cell during the experiments. A constant water pressure was supplied to the lower end of the core and the flow was recorded from the overflow at the top. The flow was measured for different compression pressures and water heads.

5.1 FRACTURE SAMPLE

5.1.1 Sampling technique

The sample was taken out using a core drill with a core barrel with an inner diameter of 191 mm. The core barrel had also the function of holding the sample together during the drilling. After that the drilling was finished, the sample was taken out gently from the core barrel. Hose clips were placed around the core to hold it together, Figure 5-1.

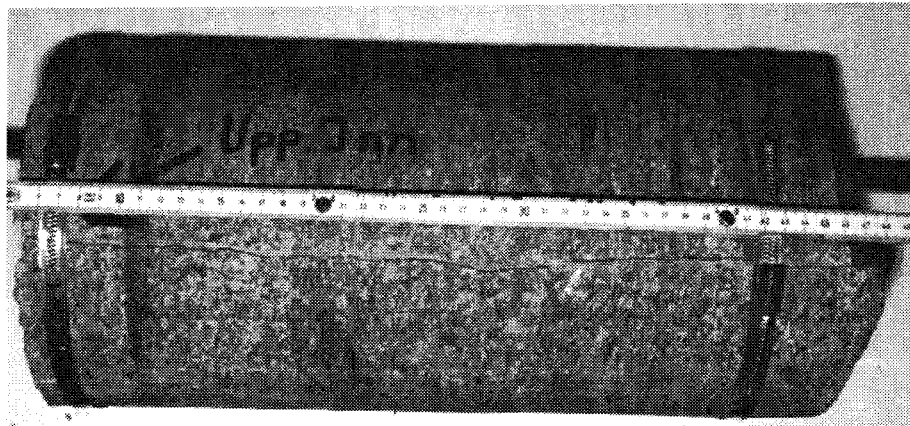


Figure 5-1. The core used in the experiments. At each end of the core is a hose clip holding the core together.

5.1.2 Description of the sample

The sample was taken from the access tunnel of the Äspö Hard Rock Laboratory in south-eastern Sweden. It was taken at section 1450, i.e. approximately 200 meters below sea level. It consists of Äspö diorite, which

is reddish grey, medium-grained, porphyritic monzodiorite, with augen 10-30 mm. The Äspö diorite belongs to the 1700-1800 Ma Småland granite suite /Wikberg et al. 1991 /.

The fracture sample was orientated in such a way that two fractures were almost parallel to the core with dips near vertical (fracture I) and horizontal (fracture II), respectively. Fracture I was conductive whereas fracture II was sealed. Originally, the plan was to study the behavior of the flow at the intersection of two fractures, but since only one of the fractures conducted water this has not been done in this study. The fracture planes of fracture I contained small amounts fracture minerals, mainly chlorite and to a minor extent calcite. From aperture measurements, it can be concluded that a small displacement has occurred along the fracture. Given the above information, the conductive fracture might be interpreted as a tensional fracture. Regarding fracture II, fracture minerals include more abundant chlorite and calcite, no aperture measurements on fracture II were undertaken.

The angle between the two fracture planes was 75° and the angle between the axis of the intersection and the axle of the core was approximately 5° . The length of the core was about 415 mm and the diameter was, as mentioned above, 191 mm. Gale /1993 / found that about 3 dm^2 or lager sample size appeared to be a representative sample of the fracture plane. According to this it can be assumed that our sample will be large enough to be representative for the fracture.

5.2 **EXPERIMENTAL SETUP**

5.2.1 **Biaxial cell**

The flow experiments were performed in a biaxial cell allowing a normal stress to be applied on the fractures. No extensive moulding or sample preparation was needed apart from the end cuts of the drill core. This was considered advantageous, since we did not want to open or disturb the natural fractures.

The cell was designed for a maximum normal stress of 10 MPa and a maximum core diameter of 210 mm. To operate the cell in a comfortable way the cell was placed in a frame where it could be rotated, Figure 5-2.

At the ends of the core, pipe collars with the same exterior diameter as the core were placed. The pipe collars were sawed to fit to the profiles at the ends of the core. With these collars, the core was lengthened to a total sample length slightly longer than the biaxial cell.

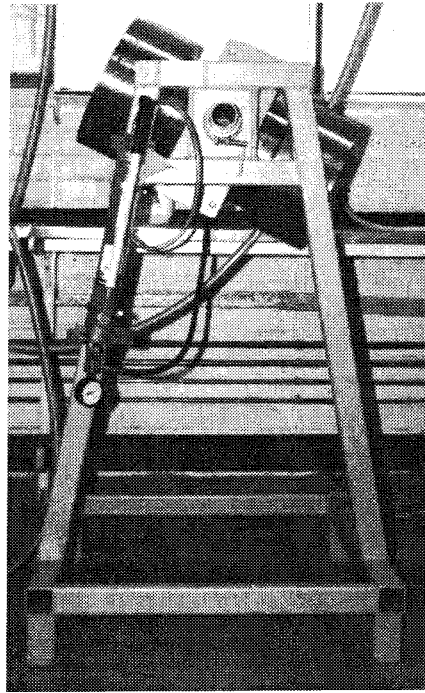


Figure 5-2. The biaxial cell used in the experiments.

5.2.1.1 Pressure distribution over the fracture

A major question is what pressure distribution we get over the fracture from the applied circular compression field from the biaxial cell. Assume that we have a fracture in the core like the case in Figure 5-3 with homogenous pressure P at the outer surface of the core and a place depending pressure $\Pi(x)$ over the fracture. The vertical component of the pressure field is $P \sin \gamma$ and the area element that it acts at is $r d\gamma dz$ while $\Pi(x)$ acts at the area element $dx dz$.

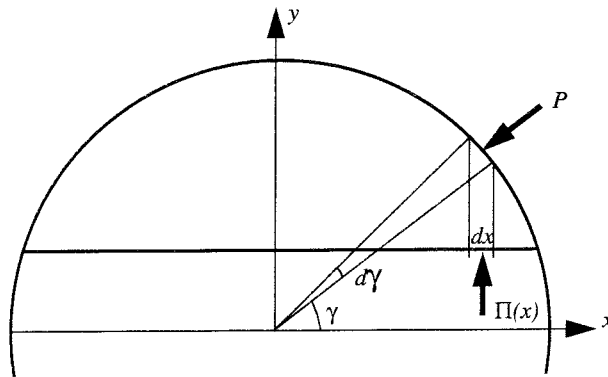


Figure 5-3. Pressure distribution over a fracture in a core with a homogenous compressive load.

Thus we get a balance equation in vertical direction:

$$P \sin \gamma r d\gamma dz - \Pi(x) dx dz = 0 \quad (20)$$

If we now express dx in cylindrical coordinates we get

$$dx = r \cos \gamma - r \cos (\gamma + d\gamma) = r [\cos \gamma - (\cos \gamma \cos d\gamma - \sin \gamma \sin d\gamma)] \quad (21)$$

which means that

$$dx \rightarrow r \sin \gamma d\gamma \text{ when } d\gamma \rightarrow 0 \quad (22)$$

If (22) is inserted into (20) we obtain

$$\Pi(x) = P = \text{constant} \quad (23)$$

for all x . Accordingly, we have a homogenous compression pressure distribution over the fracture plane.

5.2.2 Water flow arrangements

The principles of the water flow arrangements are shown in Figure 5-4. At one of the ends of the cell a gable was mounted where water could be let in. The cell was then orientated so that the gable was placed downward with a water flow upwards through the fracture. In this way the risk of getting air captured in the fracture was reduced. At the upper end we let the extension pipe stretch out over the cell and on this a spout was mounted so that the water that was flowing through the fracture could be measured.

To the gable at the lower end two vessels were connected in which the water level was constant. By a system of valves it was possible to chose which one of the vessels that supplied water to the cell. One of the vessels was vertically adjustable. By changing the level of this vessel the flow gradient over the fracture could be changed.

By changing the water supply momentary from the lower to the upper vessel it was also possible to study the time response of a an immediate change of the gradient.

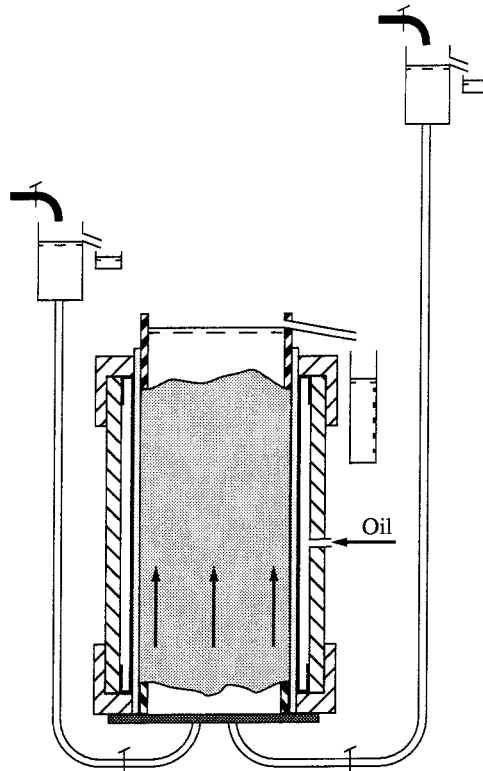


Figure 5-4. The arrangements of the flow experiments with the core in the biaxial cell.

5.2.3

Pressure measuring points

To get an idea of the distribution of the piezometric head in the fracture plane, two holes were drilled from the upper end of the core awry down to the fracture plane, Figure 5-5. To each of the holes a tube was coupled to a stand pipe with a head scale giving the possibility to read the piezometric head at the point where the hole penetrated the fracture plane.

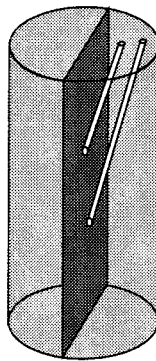


Figure 5-5. Principle of the two holes used for piezometric head measurements.

5.2.4 Displacement gauges

To measure the deformation of the fracture caused by the applied compression pressure on the core, a displacement gauge was mounted at each end of the sample.

We did not use an ordinary strain gauge because of the problems of a damage of the strain gauge that were associated with measuring over the fracture. Instead, we used a type of gauge which works by measuring the field from a movable magnetic staff. The detector which the staff goes through was mounted at one side of the fracture and a hold-on for the staff was mounted at the other side.

5.3 EXPERIMENTAL RESULTS

5.3.1 Flow, transmissivity and hydraulic aperture

The flow through the fracture was measured by collecting the overflow of water from the cell during a certain time. This was made for various gradients and compression pressures. In Figure 5-6 the flows are plotted against the water pressure head. The compression pressure is increased in stages for each load cycle. The points that make up the curve denoted 0.45 MPa are measured in next load cycle with a pressure at 0.45 MPa. The time between the load relaxations and the last measurement was about two and a half days. We can here see that we have a hysteresis in the flow even after several load cycles.

The flow is directly proportional to the gradient, which means that we have a linear flow regime in the fracture. The Reynolds number, Re , for flow between two planes is defined as:

$$Re = \frac{2e\rho v}{\mu} \quad (24)$$

Where e is the hydraulic aperture of the fracture, v the mean velocity of the fluid and μ/ρ the kinematic viscosity. This is equal to:

$$Re = \frac{2Q\rho}{W\mu} \quad (25)$$

where Q is the flow rate and W the width of the fracture. This gives $Re = 160$ as the maximum in our experiments. For rock fractures the critical Reynolds number for onset of turbulent flow commonly lies between 100 and 2300, increasing from the lower datum with decreasing wall roughness /Elswort and Doe 1986 /.

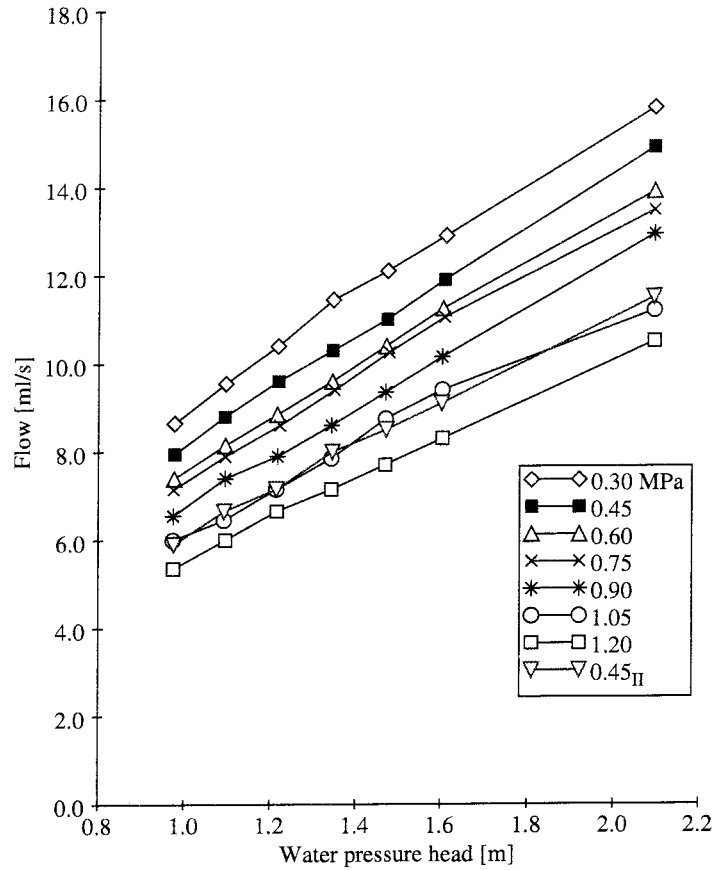


Figure 5-6. The water flow plotted against the water head for various compression pressures.

Table 5-1. Calculated transmissivity and hydraulic aperture at different pressure over the fracture. The index II stands for measurements from the next load cycle.

P [MPa]	T [m^2/s]	e [μm]
0.30	$1.81 \cdot 10^{-5}$	285
0.45	$1.67 \cdot 10^{-5}$	277
0.60	$1.56 \cdot 10^{-5}$	271
0.75	$1.51 \cdot 10^{-5}$	268
0.90	$1.40 \cdot 10^{-5}$	261
1.05	$1.27 \cdot 10^{-5}$	253
1.20	$1.15 \cdot 10^{-5}$	245
0.45 _{II}	$1.27 \cdot 10^{-5}$	253

Using the data shown in Figure 5-6 it is possible to calculate a transmissivity, T , and a hydraulic aperture, e , for each of the compression pressures. The transmissivity is calculated from Equation (2), and the hydraulic aperture from Equation (3). The transmissivities are shown in Table 5-1, together with the hydraulic apertures, are average values for the calculated transmissivity at each measured level of water pressure head.

5.3.2 Compressibility and storage coefficient

The hydraulic aperture of the fracture will decrease with 40 μm when the compression pressure increase from 0.3 to 1.2 MPa. In terms of compressibility this corresponds to a $\kappa = 2 \cdot 10^{-6} \text{ Pa}^{-1}$ for the fracture. The decrease of the mechanic aperture measured by the displacement gauges is for the actual pressure interval 27 μm and 31 μm for the bottom and top respectively.

Using the compressibility, the storage coefficient, S , can be calculated from Equation (26):

$$S = \rho g b (\omega \kappa_w + \kappa) \quad (26)$$

where b is the aperture and ω is the porosity. The compressibility for water $\kappa_w = 5 \cdot 10^{-10} [\text{Pa}^{-1}]$ can be ignored according to the compressibility of the fracture and the storage coefficient for the fracture will then be $5 \cdot 10^{-6}$.

Another way to calculate the storage coefficient of the fracture is to study the time response to a momentary change of the water head gradient. Assuming a linear variation, when the system is in equilibrium, the water head pressure distribution h over the fracture can be written as:

$$h(z, t) = h_0 + \Delta h \frac{z}{L} - \Psi(z, t) \quad (27)$$

where h_0 is the water head at the upper end of the sample, $\Delta h/L$ the gradient over the sample after a long time, L the total length of the sample, z the coordinate length the sample, and Ψ a time and place dependent variable described by the Equation system (28):

$$\begin{cases} \nabla^2 \Psi = \frac{S \partial \Psi}{T \partial t} & \text{DE} \\ \Psi(0, t) = \Psi(L, t) = 0 & \text{BC} \\ \Psi(z, 0) = \Psi_0 \frac{z}{L} & \text{IC} \end{cases} \quad (28)$$

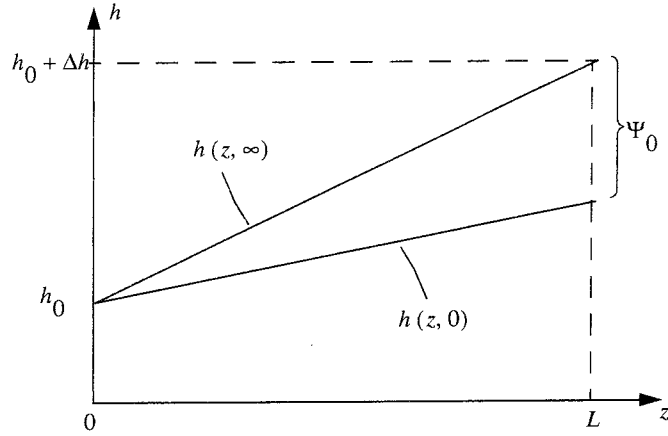


Figure 5-7. The pressure distribution over the sample for $t = 0$ and $t = \infty$.

See Figure 5-7 for an illustration of the used symbols. The differential equation with the given boundary conditions has the following solution:

$$\Psi = \sum_{n=1}^{\infty} \tilde{f}_n \sin \frac{n\pi z}{L} e^{-\frac{T}{S} \left(\frac{n\pi}{L}\right)^2 t} \quad (29)$$

Using the initial condition, the Fourier coefficients, \tilde{f}_n are calculated to be:

$$\tilde{f}_n = \frac{\int_0^L \Psi_0 \frac{z}{L} \sin \frac{n\pi z}{L} dz}{\int_0^L \sin^2 \frac{n\pi z}{L} dz} = \frac{\Psi_0/L^2 \int_0^L z \sin \frac{n\pi z}{L} dz}{\int_0^L \sin^2 \frac{n\pi z}{L} dz} = \frac{2\Psi_0}{n\pi} (-1)^{n+1} \quad (30)$$

and Equation (28) can be written as:

$$h = h_0 + \Delta h \frac{z}{L} - \frac{2\Psi_0}{\pi} \sum_{n=1}^{\infty} \frac{(-1)^{n+1}}{n} \sin \frac{n\pi z}{L} e^{-\frac{T}{S} \left(\frac{n\pi}{L}\right)^2 t} \quad (31)$$

The water head gradient at the upper end is:

$$i(0, t) = \left. \frac{\partial h}{\partial z} \right|_{z=0} = \frac{\Delta h}{L} - \frac{2\Psi_0}{L} \sum_{n=1}^{\infty} (-1)^{n+1} e^{-\frac{T}{S} \left(\frac{n\pi}{L}\right)^2 t} = \frac{\Delta h}{L} - \frac{\Psi_0}{L} D(u) \quad (32)$$

where

$$D(u) = 2 \sum_{n=1}^{\infty} (-1)^{n+1} e^{-\frac{(n\pi)^2}{u}} \quad (33)$$

and

$$u = \frac{SL^2}{Tt} \quad (34)$$

Using Equation (32) it is now possible to express the outflow during the time as:

$$Q(t) = TW \left(\frac{\Delta h}{L} - \frac{\Psi_0}{L} D(u) \right) \quad (35)$$

By matching the outflow curve, plotted against the time, with the function $D(u)$, plotted against $1/u$, it is possible to calculate the transmissivity and the storage coefficient. In Figure 5-8 the method is illustrated with data from an experiment with a compression pressure at 0.75 MPa and a difference in water pressure $\Psi_0 = 1.12$ m. Unfortunately, the response to changes of the outflow was too slow in our experiment because of the setup with a water volume between the fracture end and the outflow pipe. The transmissivities are almost the same as before but the storage coefficient is in an order of 10^{-2} which is not a reasonable value, but with another setup it would still be a practicable method.

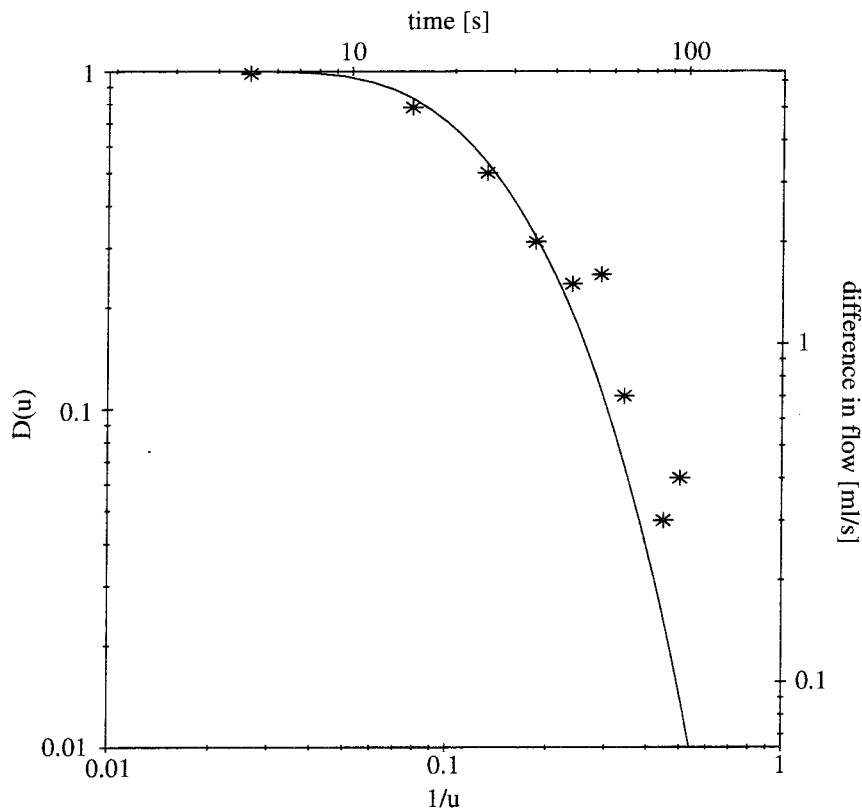


Figure 5-8. The function $D(u)$ plotted against $1/u$, used to calculate the transmissivity and storage coefficient from a momentarily change of the gradient over the fracture.

5.3.3

Tracer test

In order to estimate the transport time along the fracture, a tracer test was performed. A tracer consisting of a mixture of water and Uranine was used. The tracer was filled into the upper vessel. At the initial stage, the cell was supplied with water from the lower vessel. At a given time, the valve to the upper vessel was opened. Due to the higher water pressure of the upper vessel, the water was substituted with the tracer in the whole system, including the lower vessel and the volume between the gable and the core. The compression pressure during the tracer test was 0.45 MPa.



Figure 5-9. Video registration of tracer. a) Before the tracer has arrived. b) The moment of first arrival of tracer. c) The tracer mixed with the water above the core.

The detection of the tracer at the upper end of the core was registered by a video camera. Unfortunately, we had two different problems with the detection, both according to the fact that we had a water volume also above the core. The first problem was that the tracer was mixed with the total water volume when it first arrived so after just a few seconds it was impossible to see the core (Figure 5-9c). We tried to get around this problem by making channels by plexiglas from the fracture opening to the water surface but it was not successful, mainly because of the other problem. That was the reflection we have in the water surface from the UV-lamps and ordinary lamps that we needed to get a good view of the test in the video camera.

The tracer arrived first at a point 65 mm from the left side of the fracture (Figure 5-9b). The time for this first arrival was 3.4 seconds after the tracer was added. This corresponds to a maximal transportation velocity of 0.12 m/s. The next arrival point occurs at the right side of the fracture 4.2 seconds after the addition of the tracer and after 7 seconds the tracer had arrived over the whole fracture.

The expected time to exchange the water volume in the fracture can be calculated from the volume of the fracture divided by the volumetric flow rate:

$$t = \frac{LWb}{Q} \quad (36)$$

Using the mean aperture, b , from the aperture measurement (Chapter 6.2) the expected time of exchanging of the water volume in the fracture is 4.5 s. This corresponds to a mean velocity, v , at 0.09 m/s. Assuming that there is no adsorption, the expected concentration of tracer can be calculated as a function of location along the fracture, z , and time, t , /de Marsily 1986 /:

$$C(z, t) = \frac{C_0}{2} \left[\operatorname{erfc} \left(\frac{z - vt}{2\sqrt{\alpha_L vt}} \right) \right] \quad (37)$$

there C_0 is the initial concentration and α_L is the longitudinal intrinsic dispersion coefficient. By matching Equation (37) with the measured time for the first arrival (Figure 5-10) α_L can be estimated to 3 mm. This is of the same magnitude as the measured correlation length in the aperture measurements (Figure 6-2). In Figure 5-10 we can also see that the expected relative concentration at the time for the arrival at the second point is 30%, which means that we have a channeled flow, where 30% of the flow arrive at the first arrival point. We can also see that the measured time of 7 s for the tracer to arrive over the whole fracture, corresponds well with the expected time.

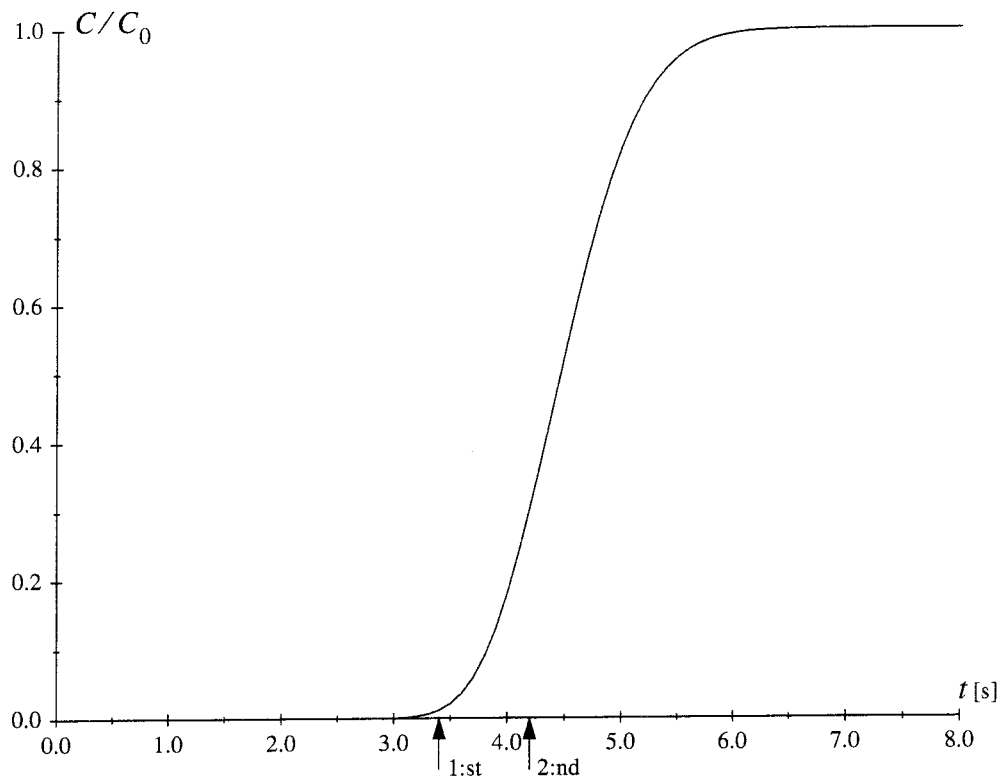


Figure 5-10. Expected concentration of tracer as function of time at the upper end of the fracture with $\alpha_L = 3$ mm. The times of 1:st and 2:nd arrival are also marked.

5.3.4 Pressure measuring points

The results from the pressure measuring points shown in Figure 5-11 are for different compression pressures. The water pressure head at the lower measuring point is what was expected if the gradient was uniform. The head at the upper measuring point, on the other hand, is higher than expected. This indicates that the aperture is smaller than the mean in the upper part of the fracture, followed by a part with a wider aperture.

The displacement of the pressure gradient when the compression pressure is changed, is general for all levels of water head at the lower end of the core. This indicates that an increase of the compression pressure influences the aperture reduction more at the lower measuring point than at the higher one. Bearing in mind the conclusion that the aperture already is smaller at the upper end of the core, this is reasonable. However, this somewhat contradicts the results from the displacement gauges, which showed that the displacement was greater at the upper end, than at the lower one,

Section 5.3.2. On the other hand, the difference between these displacements are rather small and even for the upper part of the pressure interval, the displacement is greatest at the lower end of the core.

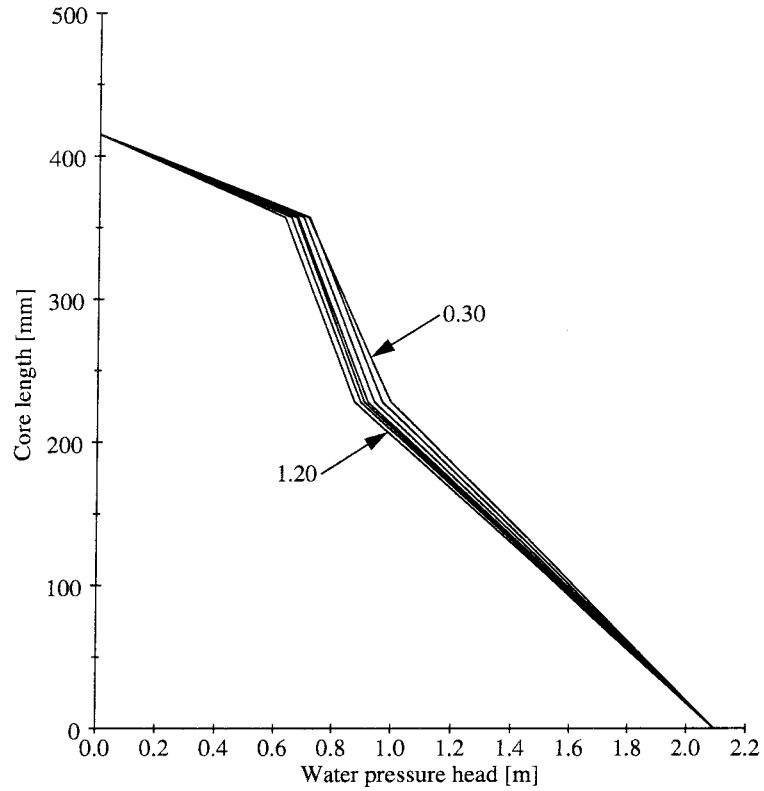


Figure 5-11. The pressure distribution over the length of the fracture based on data from the two pressure measuring points.

FRACTURE APERTURES

The fracture aperture of the sample used in the flow experiments described in Chapter 5 was measured after that the flow experiments were finished. In Chapter 7 the measured flow is compared with the predicted flow based on the geometrical description of the fracture.

The fracture was injected with fluorescent epoxy while it still was in the biaxial cell. After that the epoxy had hardened the core was cut up in slices to provide a couple of profiles along the fracture. These profiles were examined with a stereo-microscope connected to an image analysis system. A more detailed description of the aperture measurements is in Hakami and Larsson /1996 / (see also Hakami /1995 /).

6.1

GROUTING WITH EPOXY RESIN

The epoxy used to grout the fracture was Epofix (for technical data of Epofix, see appendix 3). This is an epoxy with well-known behavior together with rock material. It is frequently used for the preparation of microscopic thin sections. One important property for our experiment is that it has an insignificant hardening shrinkage. This is important because we are using the thickness of the epoxy layer as a measurement of the fracture aperture. To get a lower viscosity of the epoxy acetone was added. The mixing ratio in volume percentage of resin, hardener and acetone respectively is shown in Table 6-1 compared to the normal mixing without acetone. To make the epoxy fluorescent Epodye was used as dye.

Table 6-1. Mixing ratio of the epoxy in volume percentage.

	Resin	Hardener	Acetone
Used	66%	22%	12%
Normal	89%	11%	-

The epoxy was injected in the fracture while the core was still sitting in the biaxial cell. The compression pressure over the sample during the injection and the hardening time was 0.45 MPa. The cell was rotated upside down compared to the orientation during the flow experiments. Epoxy was filled between the core and the gable and compressed air was used to get an injection pressure of 50 kPa. The injection pressure was held on until epoxy

had arrived over the total fracture opening at the other end of the fracture. Sixty-five hours after the grouting was made, the confining stress over the sample was released and the core was taken out of the biaxial cell.

6.2 APERTURE MEASUREMENTS

The aperture measurements were made by Eva Hakami at the Division of Engineering Geology, Department of Civil and Environmental Engineering, Royal Institute of Technology /Hakami and Larsson 1996 /. Using a diamond disc cutter the core was cut into segments and these segments were moulded in concrete. Each part was then cut along profiles across the fracture. After each cut, aperture measurements were made along the exposed fracture profile using a stereo-microscope directly connected to an image analysis system. With the aid of microscope filters, it was possible to obtain good contrast between the rock and the fluorescent epoxy. The image analysis system was programmed to measure the aperture at points with a specified distance along the profile. The accuracy of the measurements was about 10-30 μm with the image size used. At points where the fracture had two epoxy layers an equivalent aperture was calculated as $b = \sqrt[3]{[b_1^3 + b_2^3]}$. The term aperture is in this study defined as the separation distance between the fracture surfaces in the normal direction to a plane parallel to the fracture. The aperture is thus a pointwise distribution of values ranging from zero to a maximum value. Note that because of the roughness, the aperture is not the shortest distance between the two fracture surfaces at each point. However, the fracture plane have to deviate from the reference plane with more than 8° if the difference between the aperture and the shortest distance should be more than one percent. The contact area is here defined as the areas where the apertures are smaller than a certain threshold.

The configuration of the measurements taken on the studied fracture area is shown in Figure 6-1a. The area was divided into eight subareas, A-H. The aperture measurement points were taken with distance of 200 μm for 65 profiles, 100 μm for four profiles and 50 μm for one profile. A total of some 30 000 aperture data were recorded. The direction of profiles was changed between subareas in order to be able to pick up any possible anisotropy in the aperture pattern.

The spatial distribution of the aperture is understood by posting the location of data points with an aperture smaller than 50 μm (Figure 6-1b). It can be seen that these contact areas are more frequent to the upper end and the right side of the specimen. This corresponds to the results from the tracer test in Chapter 5.3.3 where we found that the tracer first arrived at the left-hand side and the result in Chapter 5.3.4 where it was noticed that the pressure fall was greatest at the upper end of the fracture. The locations of first and second arrival point in the tracer test are marked in Figure 6-1b, and the locations of the pressure measuring points are marked in Figure 6-1a, respectively.

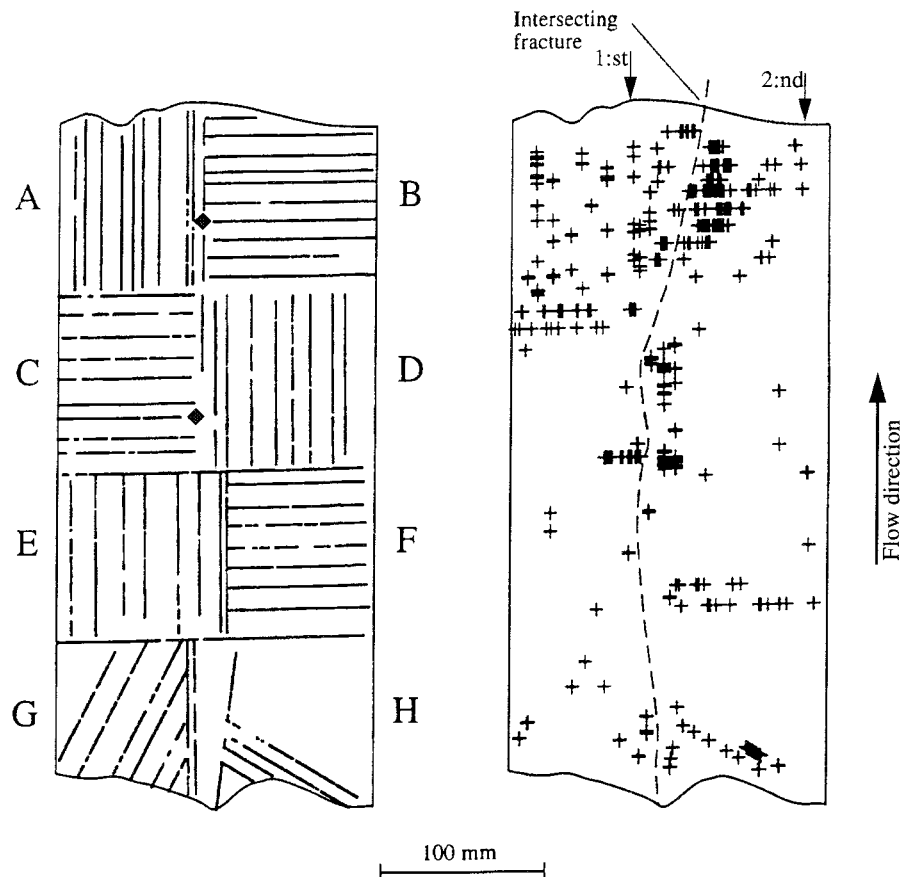


Figure 6-1. a) Configuration of measurement profiles and subareas. The locations of the pressure measuring points (Chapter 5.2.3) are marked with ◆. b) Location of measurement points with apertures smaller than 50 μm. The locations of 1:st and 2:nd arrival point in the tracer test (Chapter 5.3.3) are also marked.

The contact areas are correlated to the fracture intersection, (dashed line in Figure 6-1b), in particular subarea B. In Subareas D, E and G the measurement profiles are oriented subparallel to the intersection and therefore the location and character of the intersection is not well known in the lower part of the fracture. No epoxy has been noticed in the intersecting fracture except at the intersection with the studied fracture.

The results of the aperture measurements of the eight subareas are presented as summary statistics in Table 6-2. In Figure 6-2 frequency histograms and variograms for each subarea are shown. The arithmetic mean of the subareas ranges from 307 μm to 380 μm, and the standard deviation lies between 133 μm and 321 μm. In general, the shape of the frequency distributions is similar for all samples. The distributions are bell-shaped with a few percentage zero-apertures. Compared to a normal distribution they have a somewhat higher peak around the median. The mean apertures are slightly

Table 6-2. Statistics of apertures in the subareas of the fracture.

Subarea	a	b	c	d	e	f	g	h
Number of data points	5836	5825	3525	3840	3220	3468	2423	1679
Mean aperture	365	307	380	349	384	358	379	360
Standard deviation	133	133	151	145	157	150	207	231
Median	366	317	373	338	358	331	336	321
$b < 50 \mu\text{m}$ [%]	5.5	7.0	3.0	3.5	0.5	0.7	0.7	3.0

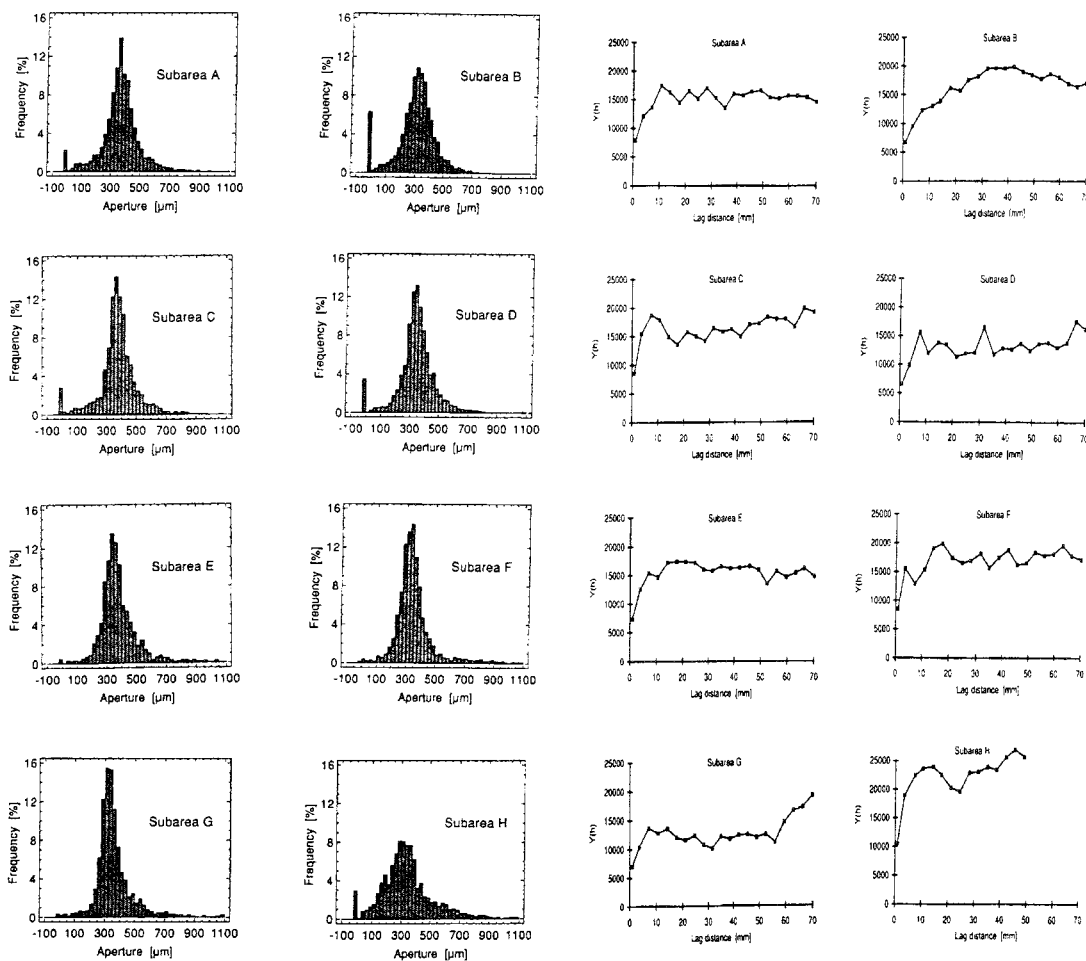


Figure 6-2. Aperture distribution and experimental variograms for the eight subareas of the studied fracture.

larger on the left-hand side of the fracture. Also, the apertures are slightly larger at the inflow side compared to the outflow side. Out of the total aperture data recorded, about 15% were taken at points with more than one

epoxy layer. In the calculations of the variograms, apertures in the interval 0-1500 μm are included. For all samples, the range of the variograms is in the interval 5-20 mm. The range is largest in the subarea B where the contact area is also largest. The variograms for the studied fracture may be fairly well approximated with an exponential model with a range of about 8 mm and a sill of about 16 000 μm^2 . The trend in the aperture with slightly higher values to the left and to the inflow side of the fracture is indicated in some of the variograms where the variograms increase with lag distance without staying at a plateau. However, since this trend is small compared to the mean aperture of the fracture, it does not have a significant influence on the shape of the variograms or the interpreted correlation lengths.

MODELLING OF THE FLOW EXPERIMENTS

7.1 FDM-MODELING OF THE FLOW

Using the aperture measurement data presented in Section 6.2 the flow through the fracture has been calculated using the FDM-model in a similar way as in Chapter 4.

We have the same basic conditions which means that transmissivity values are needed in a regular grid parallel to the orientation of the fracture. Even if most of the measurement profiles are parallel or at right angles to the fracture orientation, they are not regular. To overcome this problem, the fracture plane was divided in several small subareas, each one 25x25 mm. For each subarea the mean and standard deviation of the aperture have been calculated. Also the ratio of measurements of contact areas for each subarea was calculated. For those subareas, where no measurement data exist, the measurements from the closest subarea were used, see Figure 7-1.

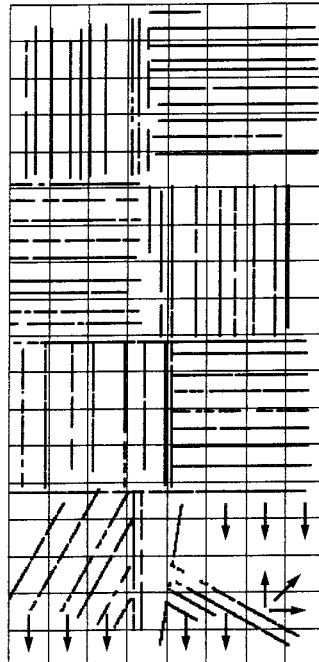


Figure 7-1. View over the subareas used to generate statistical data of the aperture distribution to the FDM-model. The arrows indicate subareas without measurement data.

For each subarea, 25 cells were given an aperture from the statistics for that subarea. This means that the cells are of the size of 5x5 mm. This is in the same order as the lag distance, see Figure 6-2, which means that it is correct to let the aperture of the cells be independent of each other.

A set of realizations of the aperture distribution was done with the same boundary conditions as in the flow experiments and with a water pressure head of 2.1 m at the lower end. The realizations gave a mean flow through the fracture of 28.1 ml/s with a variance of 1.0. However, the modelled fracture is somewhat wider and longer than the actual fracture. To compare the modelled flow with the measured one, we have to compensate for this, and we get a mean flow of 24.7 ml with a variance of 0.9. The measured flow through the fracture that we have to compare with was 11.5 ml/s, i.e. an overestimation of the flow of 2.1 times.

The reason for the overestimation can be related both to the specific fracture and the technique in general. Technical reasons might include the existence of flakes which have not been noticed when the aperture measurements were done, which means that the active aperture is smaller than the measured value. Possible air or chemical reactions in the fracture will reduce the measured flow compared to the estimated one. Another possible technical reason is that the resin may have taken away some material from the fracture. Reasons related to the specific fracture can be anisotropy or local parts of the fracture that do not play an active part for the flow regime. However, neither anisotropy nor locally isolated parts have been noticed for the studied sample.

In Figure 7-2 contour lines for the gradient in four realizations are shown. We can see that the lines in the uppermost part have a trend to be more close to each other, particularly at the right side. This corresponds with earlier results (Chapter 5.3.3, 5.3.4 and 6.2) where it was noticed that the pressure head fall was greatest in the upper (middle) part where most of the contact area was measured and where the tracer arrived last. This result is also illustrated in Figure 7-3 where a series of head gradients over the length of the fracture is shown for one of the realizations. Figure 7-3 can be directly compared to Figure 5-11.

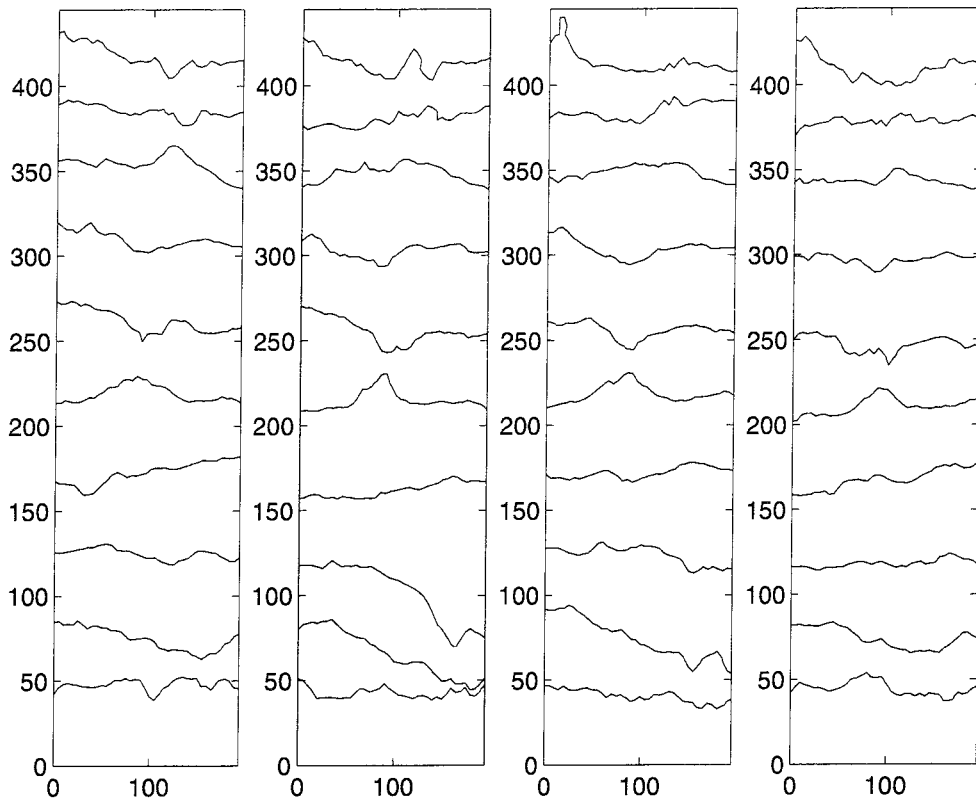


Figure 7-2. Contour lines for the pressure over the fracture in four realizations.

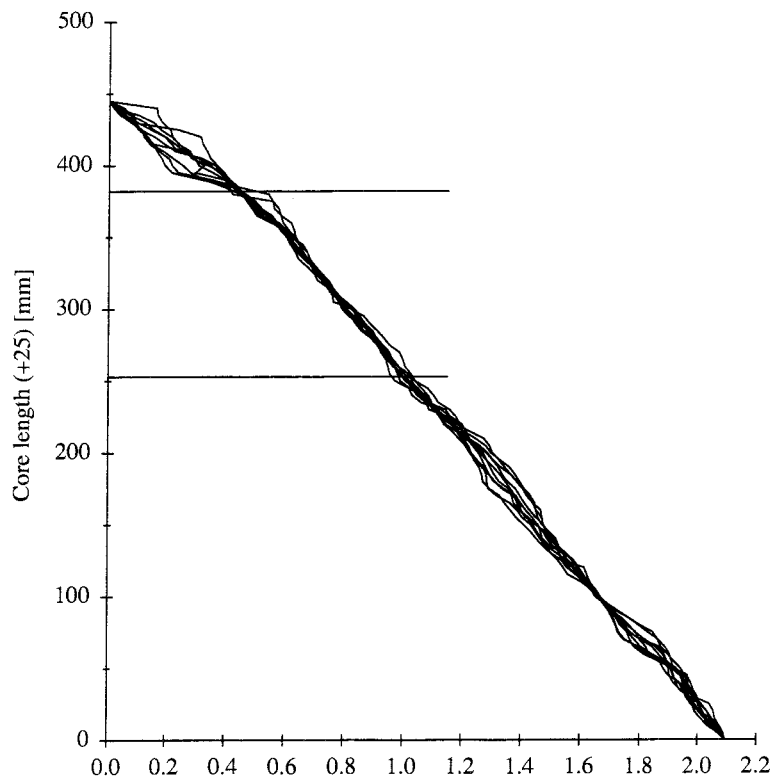


Figure 7-3. Examples of pressure distribution over the length of the fracture in one of the realizations. The location of the pressure measuring points in the experiment are marked.

7.2 TRACER SIMULATION

Using the particle tracking algorithm described in Chapter 4.2, the tracer experiment in Chapter 5.3.3 has been simulated. The average time for first arrival was predicted to be 2.4 s which should be compared with the measured time of 3.4 s. This means that the maximal transportation velocity was overestimated with a factor 1.4. The transportation velocity is thus somewhat better estimated than the flow, even when taking into account the fact that the flow depends on the cube of the aperture and the velocity depends on the square.

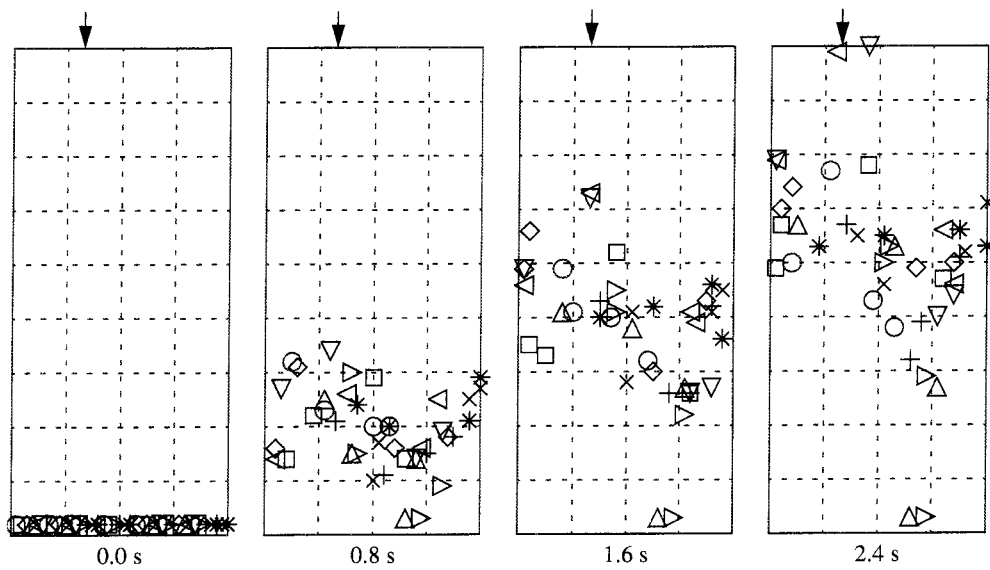


Figure 7-4. Different time steps in a simulation of the tracer experiment described in Chapter 5.3.3. The location of first arrival in the experiment are marked.

In Figure 7-4 the canalization of the flow can be noticed. The particle velocity is smaller at the right side and at the upper left side due to the more closed parts of the fracture in these regions. The two particles which have not left their injection points were placed in contact area cells. It can also be noticed that there is good correlation between the location of the first arrival in the experiment and in the simulation.

7.3

ESTIMATION OF THE FLOW BASED ON THE APERTURE MEASUREMENTS

Using the statistical data of the fracture aperture, the effective transmissivity can be estimated by using the different equations given in Chapter 2.1. The various predictions are listed in Table 7-1. The arithmetic mean of the cube of the aperture is, as mentioned, the upper bound on the actual transmissivity and it will greatly overestimate the transmissivity, even if corrected for the contact area. The cube of the mean of the aperture is somewhat more accurate, and the geometric mean of the aperture is further better. The most accurate prediction, is made by Equation (7) in conjunction with the correction for contact area, Equation (10). However, the prediction still overestimates the effective transmissivity, and consequentially also the flow, with a factor 2.2. This means that the FDM-modelling estimates the flow somewhat better, but the accuracy is in the same order of magnitude.

Table 7-1. Prediction of hydraulic transmissibility (divided by $\rho g/12\mu$). $E[b]$, σ_b and e are given in units of 10^{-6} m; c is dimensionless; other values are in units of 10^{-12} m³.

	Value	Comments
$E[b]$	366	mean aperture
σ_b	148	standard deviation of the aperture
e	253	hydraulic aperture
c	0.027	contact area extent
$E[b^3]$	83.3	upper limit
$E[b^3](1-2c)$	78.8	as above, adjusted for contact areas
$E[b]^3$	49.1	cube of mean aperture
$E[b]^3(1-2c)$	46.1	as above, adjusted for contact areas
b_G^3	39.2	geometric mean, Eq (8)
$b_G^3(1-2c)$	37.0	as above, adjusted for contact areas
$E[b]^3(1-1.5\sigma_b^2/E[b]^2)$	37.1	Eq (7)
$E[b]^3(1-1.5\sigma_b^2/E[b]^2)(1-2c)$	35.1	as above, adjusted for contact areas
e^3	16.2	calculated from T

SOME NOTES ON TWO-PHASE FLOW IN FRACTURES

One of the problems that affect the inflow to, and the groundwater-pressure around, a tunnel is that it exists both water and air in the fractures close to the tunnel. In a fracture with varying aperture, the gas will go to the widest part of the fracture because of the capillarity. The most permeable parts of the fracture are thus filled with air and cannot conduct water, and the total permeability decreases.

Therefore, two-phase flow, or partially saturated flow, was studied which involves the movement of two fluids, air and water. The movement of the air is usually neglected because of its much lower density. As a result of this, only the continuity equation of water is considered.

8.1 THE PRINCIPLES OF TWO-PHASE FLOW

The flow q of a liquid through a (saturated) medium is described by the Darcy equation:

$$q = -Ki \quad (38)$$

where i is the gradient of the total potential and K is the hydraulic conductivity which depend of the liquid and the permeability k of the medium:

$$K = \frac{k\rho g}{\mu} \quad (39)$$

If the medium is not completely filled with only one liquid, the medium is considered to be unsaturated with respect to that liquid. The saturation, S , is for a porous medium defined as (volume of water)/(total pore volume). A similar term to the saturation is moisture content, θ , which is defined as (volume of water)/(total volume of sample). The saturation may vary from 0 to 1, or from 0 to 100%, and the moisture content may vary from 0 to the total porosity ω .

The character of the saturation is dependent upon the nature of the second fluid which occupies the space vacated by the homogeneous liquid. If the second fluid is a mixture of gases, such as air, then the resulting three-phase system becomes the one which is meant with unsaturated flow. The degree of unsaturation has profound influence on the physics of flow of water (and gas) in the system. At low degrees of saturation of either water or gas, the

respective phase ceases to be continuous and exists in the medium in the form of isolated pendular bodies of water or entrapped air bubbles (Figure 8-1). It is clear that a continuum description of water flow is dependent of the assumption that water forms a continuous phase /Rasmuson, 1989 /.

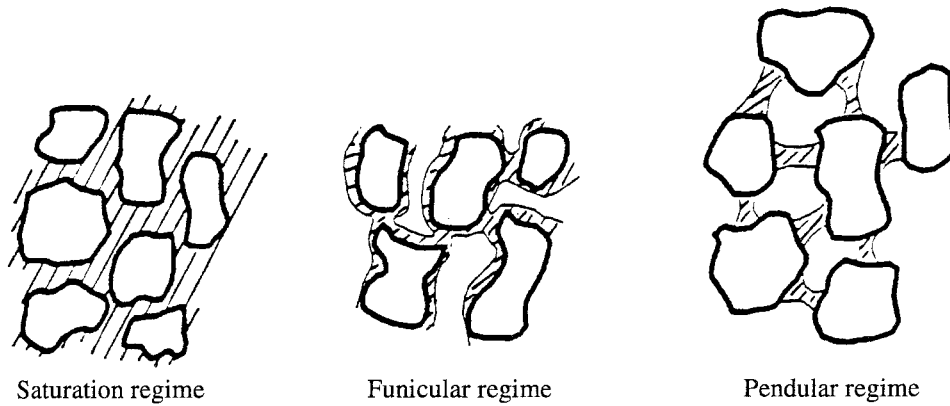


Figure 8-1. Three different water saturation regimes /Rasmuson, 1989 /.

In a partially saturated porous medium, only the pores that contain fluid can conduct fluid /Matanga and Frind, 1983/. The hydraulic conductivity of the medium therefore follows a curve similar to that of saturation (Figure 8-2). However, when the draining of an initially saturated medium commences, it is the largest pores that drain first because the capillary pressure, P_c , in these pores is the lowest. In consequence, the hydraulic conductivity distribution generally experiences a sharp drop initially followed by a more gradual decline.

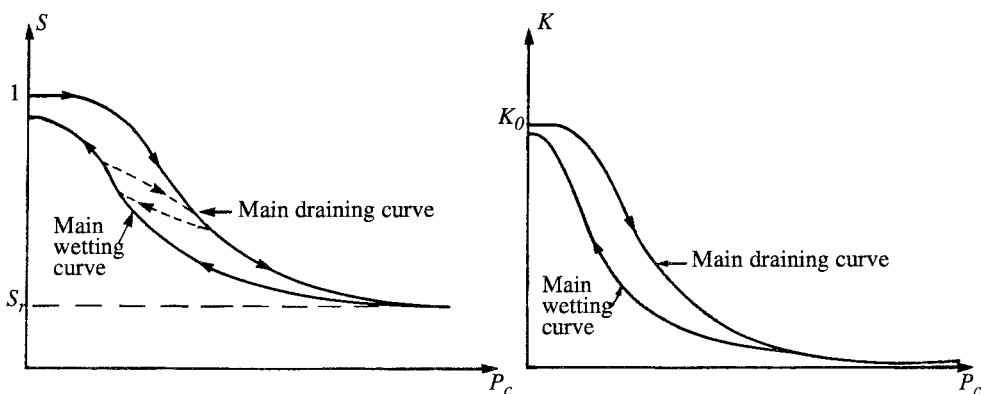


Figure 8-2. The saturation and the hydraulic conductivity as functions of the capillary pressure.

Rasmuson /1978 / have listed three reasons for this behavior:

- The total cross section available for flow decreases with the saturation.
- The largest pores are emptied first as the saturation decreases. Since the contribution to K per unit area varies roughly as the square of pore "radius" (Poiseuille's law), K can be expected to decrease much more rapidly than the saturation.
- As the saturation decreases, the probability increases that water will occur in pores and wedges isolated from the general three-dimensional network of water films and channels.

In Figure 8-3 we can see how the relative permeability curves of a wetting and a non-wetting fluid in principle vary with the saturation of the wetting fluid. S is the saturation of the wetting phase and k_r the relative permeability. S_r is the irreducible saturation of wetting phase (pendular rings, etc.) and S_m is the saturation of the non-wetting phase at which it is reduced to unconnected bubbles.

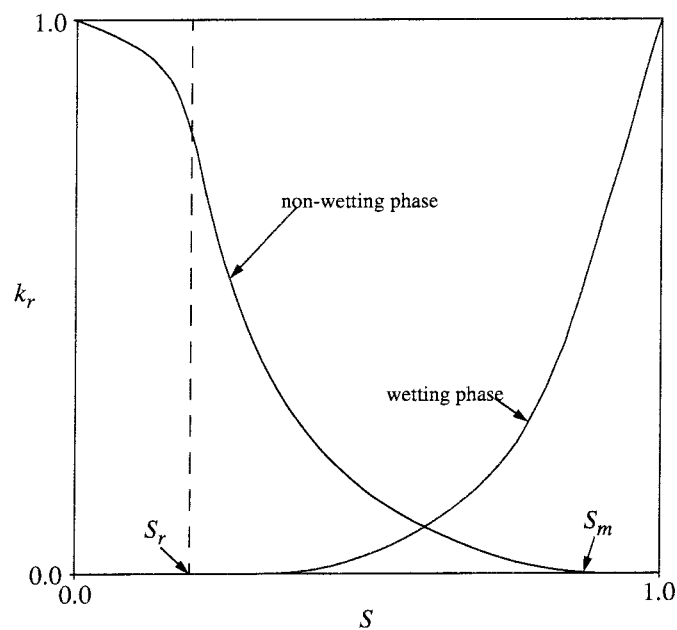


Figure 8-3. Typical relative permeability curves (after Gustafson and Åberg /1985 /).

It is however worth to notice that there is no fundamental correlation between the permeability and porosity of a porous medium. A medium with large porosity can have small permeability if the pores are to a large extent

unconnected. The permeability and also the capillarity mainly depend on the size of the pores and much less on the porosity of the medium /Gustafson and Åberg, 1985 /.

Yortsos and Fokas /1983 / have developed an one-dimensional linear model that includes the effects of capillary pressure. They studied a water/oil displacement process with constant injection rates. This is a method named waterflooding used in the petroleum industry to increase the total withdrawal of oil. The mobility ratio has the functional form:

$$\frac{k_{ro}\mu_w}{k_{rw}\mu_o} = F \left(\frac{S - S_{or}}{1 - S_{wr} - S} \right) \quad (40)$$

where S is the oil saturation, F is a parameter that can be taken as the water-to-oil viscosity ratio and the subscript r stands for residual values. They have also described the oil saturation distribution as a function of position and time in terms of F and a dimensionless parameter, β , that denotes the relative magnitude of viscous to capillary terms. This is not exactly applicable to our problem but it illuminates some of the parameters that are involved.

Another factor is the wettability of the surfaces of the media. Contact angle is the most universal measure of the wettability /Norman, 1990 /.Figure 8-4 shows idealized examples of contact angles at smooth solid surfaces for oil and water of matched density. The wettability may be different when a fluid-fluid interface is advancing or receding on a solid surface. This phenomenon is called hysteresis (Figure 8-5).

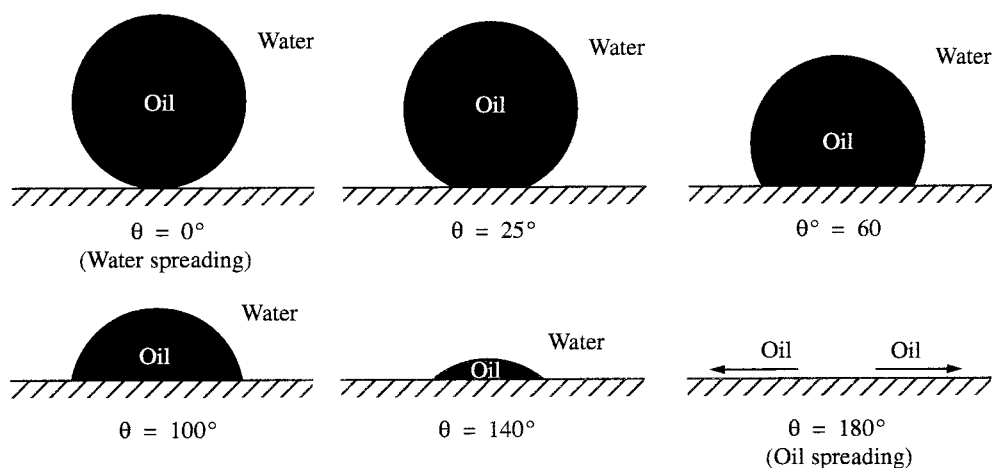


Figure 8-4. Idealized examples of contact angles and spreading. After Norman /1990 /.

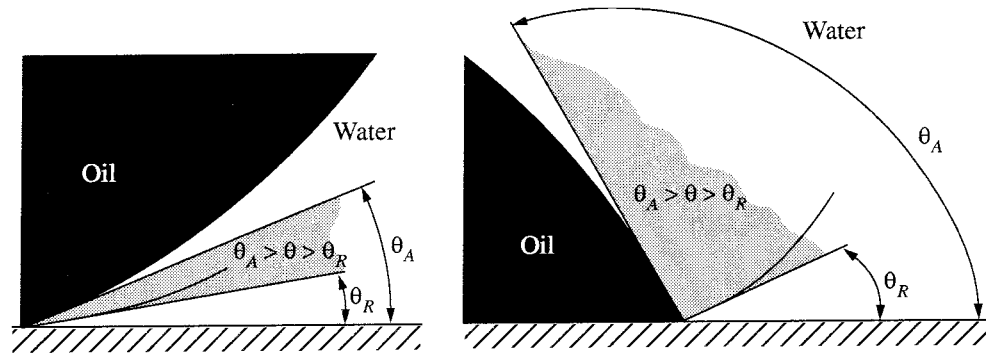


Figure 8-5. Possible ranges of stable contact angle, θ , for small and large hysteresis of contact angle /Norman, 1990 /. θ_A and θ_R stands for advancing and receding contact angle, respectively.

8.2 THE EFFECT OF EXTINCTION OF HIGHLY CONDUCTIVE CELLS

We have already noticed that if air enters the system, it is the largest pores, or in the case of crystalline rocks, the widest fractures, which will dry up first. Using our numerical model described in Chapter 3.2, we have successively replaced the highly conductive cells with very low conductivities. The result for the discrete case is that the effective conductivity decreases linearly with increasing variance (Figure 8-6).

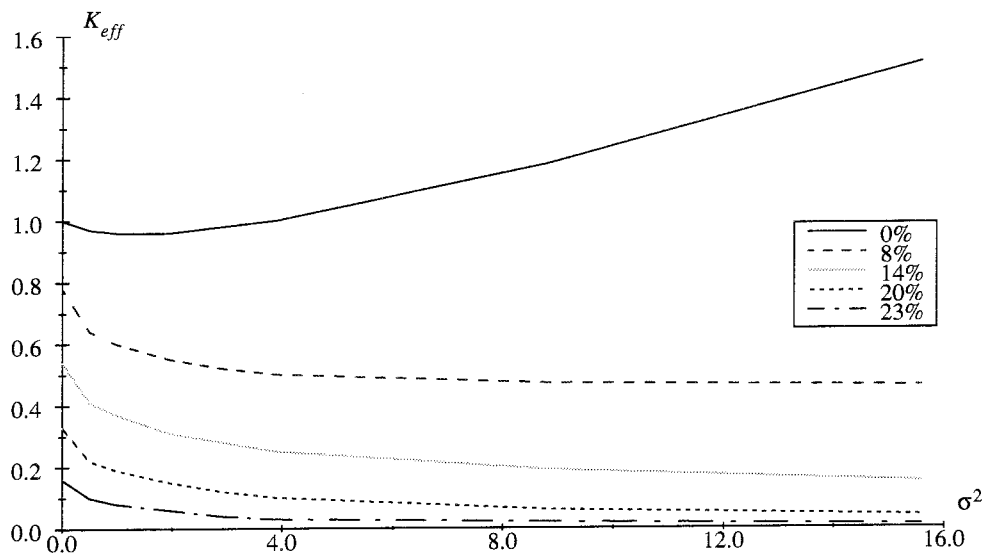


Figure 8-6. The effective conductivity as a function of the variance with the most 0, 8, 14, 20 and 23% conductive cells extenuated. Relative conductivities calculated with constant cell conductivities.

It is important to note that the variances we are discussing are calculated before the conductivities are reduced and not afterwards. That would have given a totally different result because we would have a truncated log-normal distribution after the reduction.

In the case of a linear variation of \sqrt{K} we have a weak increase of the conductivity for high variance and moderate extinction (Figure 8-7).

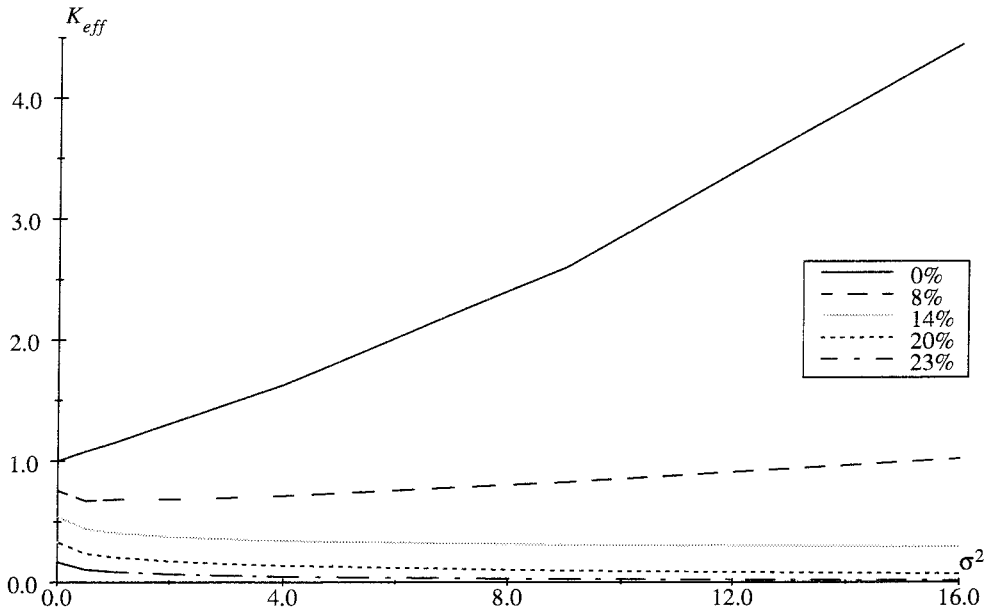


Figure 8-7. The effective conductivity as a function of the variance with the most 0, 8, 14, 20 and 23% conductive cells extenuated. Relative conductivities calculated with linear variation of \sqrt{K} .

If we look at how the effective conductivity varies with the saturation, S , for different variances, instead of how it depends of the variance with different degrees of extinction, we can compare our results (Figure 8-8) with the curve in Figure 8-3. We see that the behavior is as expected.

It is possible to approximate these curves with a power function:

$$K(S) = K_0 S^n \quad (41)$$

In our case the exponent n will vary between 4 and 20, and it will increase with the variance of the simulated conductivities.

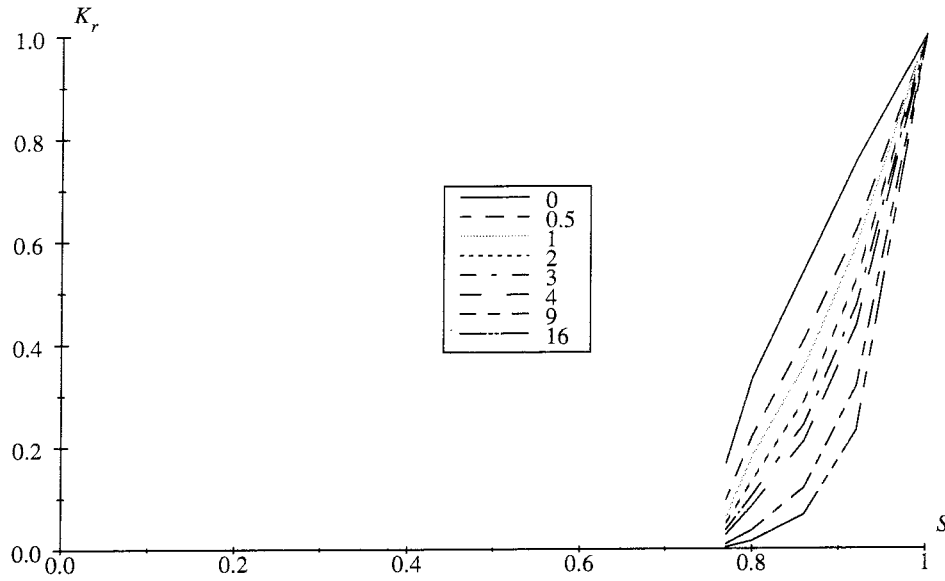


Figure 8-8. The effective conductivity as a function of the saturation with eight different variances. The relative conductivities are calculated with linear variation of \sqrt{K} .

8.3 SKIN EFFECT CAUSED BY GAS LIBERATION

When the pressure in a liquid decreases dissolved gases can be liberated. The solubility for a gas in a liquid is directly proportional to the pressure. We have previously demonstrated that the conductivity of the rock can be affected by partial gas filling of the system, which might be explained by gas liberation. It means that the gas which has been solved in the water is released when the pressure is falling near to the tunnel, and we get a zone around the tunnel with a two-phase flow.

Assume a zone with radius r_2 around a tunnel with radius r_w , where the conductivity is K/δ , whereas it is K in the rest of the rock. If we write the drawdown of the pressure at the wall of the tunnel as s_w and the difference of the pressure at the wall of the tunnel and at the border of the influenced zone, that means the drawdown difference to which gas release starts, at the radius r_2 as s_g we can calculate them as:

$$s_w = \frac{Q/L}{2\pi K} \left(\delta \ln \frac{r_2}{r_w} + \ln \frac{R_0}{r_2} \right) \quad (42)$$

and:

$$s_g = \frac{Q/L}{2\pi K} \delta \ln \frac{r_2}{r_w} \quad (43)$$

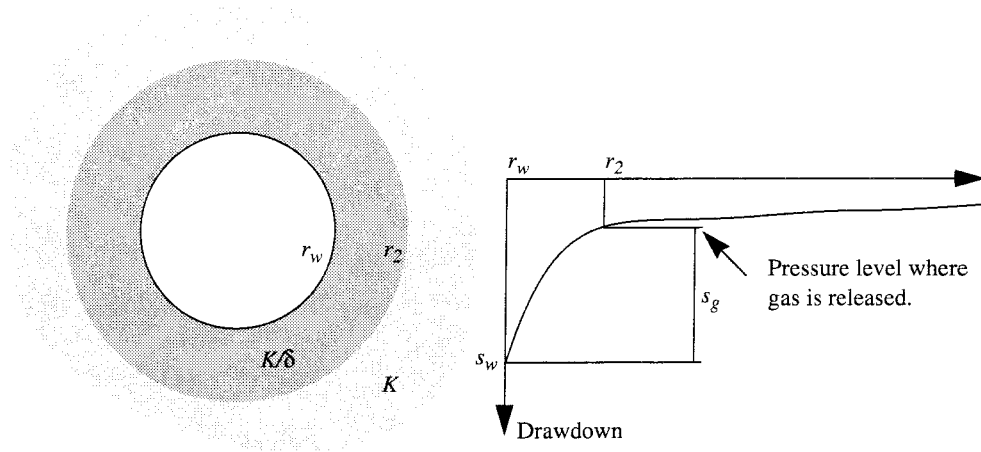


Figure 8-9. A tunnel with a conductivity K/δ in a zone around it and K in the rest of the rock.

We can also express s_w with a skin factor ξ . This gives:

$$s_w = \frac{Q/L}{2\pi K} \left(\ln \frac{R_0}{r_w} + \xi \right) \quad (44)$$

We can now solve ξ as

$$\xi = \frac{\ln (R_0/r_w)}{\frac{s_w}{s_g} \left(\frac{\delta}{\delta-1} \right) - 1} \quad (45)$$

If we instead of the skin factor look at the productivity index which is common in the oil industry we get

$$I_p = \frac{Q_{\text{with skin}}}{Q_{\text{without skin}}} = \frac{\ln (R_0/r_w)}{\ln (R_0/r_w) + \xi} = 1 - \frac{\delta-1}{\delta} \frac{s_g}{s_w} \quad (46)$$

We have seen earlier that we get a great reduction of the conductivity even for a moderate extinction of cells which means a high δ . On the other hand, from Equation (46) we can see that the value of δ is not very important if δ is large. Instead, it is the value of the ratio s_g/s_w which is significant.

A reduction of the conductivity near a wall of a tunnel can accordingly give rise to a reduced outflow, but it is not the magnitude of the conductivity reduction that is important. Gas saturated groundwater, which means that $s_w \sim s_g$, thus can mean considerable reduction of the flow.

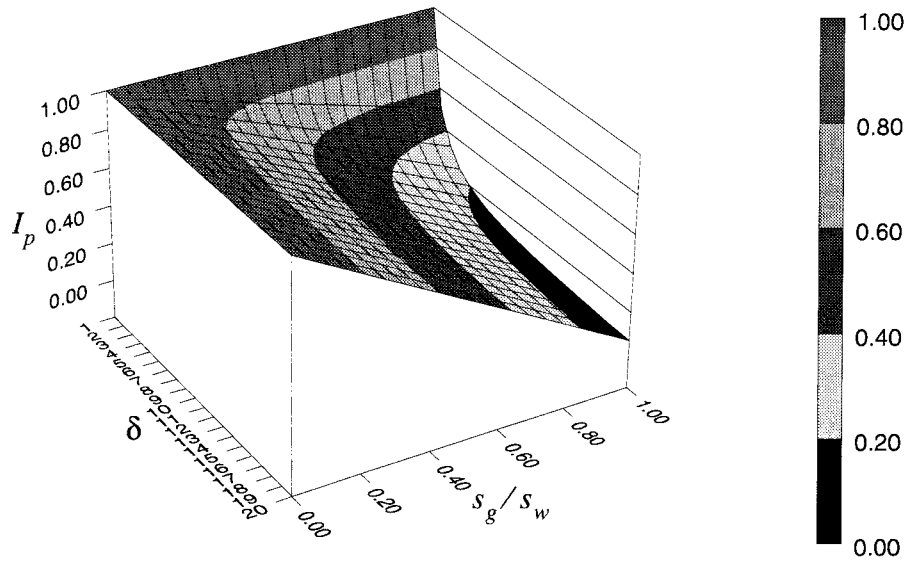


Figure 8-10. The influence of different values of δ and s_g/s_w on the productivity index I_p .

8.4

EFFECTS OF FLOW-DEPENDING SATURATION

A couples of flow-measurements which indicate that there is an instable flow to an open tunnel have been performed, see for example Olsson /1992 /. The following discussion, based on simple assumptions about the dependence between flow and saturation, might explain how it occurs.

The flow according to Darcy's law can be written as

$$Q = -K(S) i \quad (47)$$

where the conductivity depends on the saturation, S , in accordance to expression (41).

It is possible to imagine different types of the relationship between the flow and the saturation. One simple, but reasonable, relation is:

$$S = (1 - \zeta Q) \quad (48)$$

which brings Equation (47) and (41) to give:

$$Q = -K_0 (1 - \zeta Q)^n i \quad (49)$$

What we get is a feed-back of the flow on the conductivity. Equation (49) is not explicitly soluble according to q but we can get an iterative solution (Figure 8-11). If we do so, we can see that up to a certain value of ζ we have

a stable solution, but exceeding this value, which depends on the exponent n , will lead to an instable solution where the flow can fluctuate between two different values.

This explanation can be valid to some of the problems that have been registered in Stripa /Olsson, 1992 /, where great differences in the flow have been measured when the same experiment was repeated (Figure 8-12).

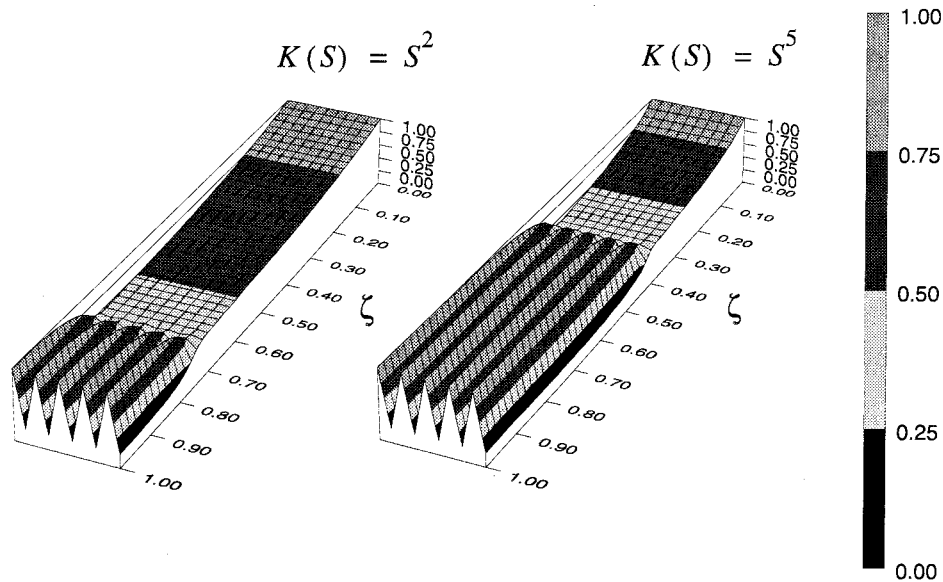


Figure 8-11. Interactive solutions of the flow in Equation (49) with $n = 2$ and $n = 5$, respectively. $K_0 = 1$

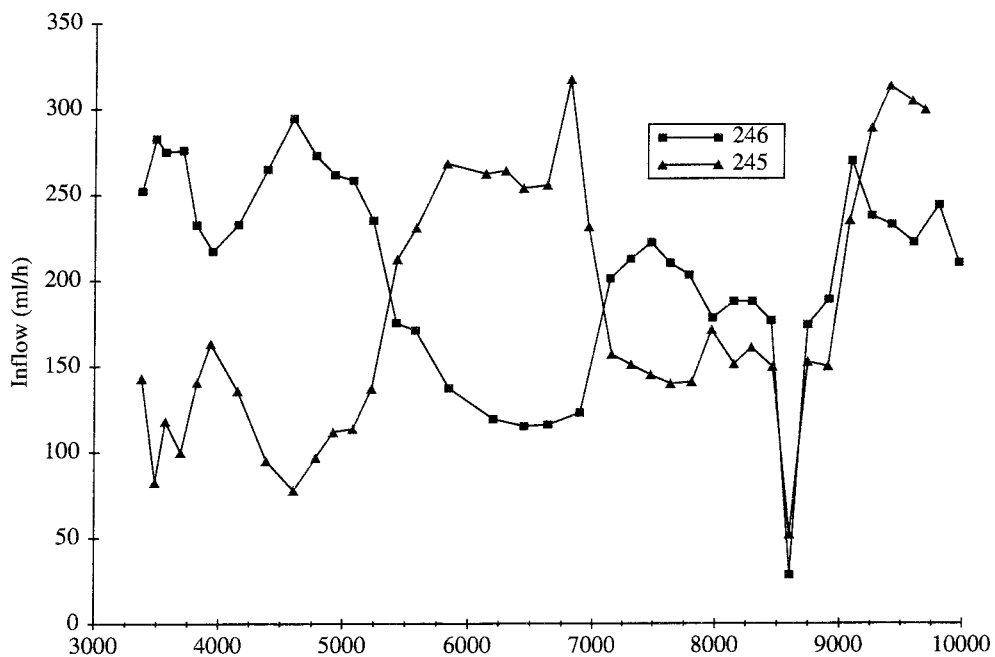


Figure 8-12. Inflow to two grid elements at Stripa as a function of time. The dip at 9000h is due to a temporary removal of packers (after Olsson, /1992 /).

CONCLUSIONS

The used FDM-model has been used with several approaches to the connection between the cells in the model. Using the geometric mean of the conductivities in two adjoining cells as the relative conductivity between the cells, gave the best agreement with the expected conductivity in both two- and three-dimensional flow. A probable reason to this is that the flow between two cells is two- rather than three-dimensional and the geometric mean of the conductivity is the theoretical solution of the effective conductivity for a two-dimensional flow.

We have also shown that the gradient field is smoother than the field of the flow, which in turn is smoother than the conductivity field. This means that the expected value of the flow is smaller than the product of the expected values for the conductivity and for the gradient.

The mean aperture of the studied fracture was 360 μm with a standard deviation of 150 μm , at a normal stress of 0.45 MPa. The hydraulic aperture at the same normal pressure was 253 μm , which means that the ratio between the mean and the hydraulic aperture was 1.4.

Using different analytical estimations of the effective transmissivity, we got an overestimation from 5.1 down to 2.2 times the measured transmissivity in the flow experiment. The most accurate estimation was obtained if we take care, not only of the mean aperture, but also of the standard deviation of the aperture and the amount of contact areas.

Using the same aperture measurement data in numerical simulations of the flow gave an overestimation of the effective transmissivity of 2.1 times. This means that we can obtain an accurate estimation of the total flow through a fracture both with our numerical model and with an analytical model. However, for estimations of the flow distribution we are restricted to use numerical models.

In the case of unsaturated flow, we have established that the flow system is strongly affected. It appears as extinctions of highly conductive parts of the system. Assuming a flow-depending saturation gives an unstable flow which can fluctuate between different values.

The gas liberation because of pressure fall in the disturbed zone around a drift causes skin effects but the magnitude of the conductivity reduction is not as important as the ratio between the drawdown of the pressure at the wall and the pressure at which the gas release begins.

REFERENCES

SNV = National Swedish Environmental Protection Board

Bakr A A, Gelhar L W, Gutjar A L & MacMillan J R, 1978. Stochastic analysis of spatial variability in subsurface flows 1. Comparison of one- and three-dimensional flows. *Water Resources Research*, Vol 14, No 2, pp 263-271

Dagan G, 1979. Models of groundwater flow in statistically homogeneous porous formations. *Water Resources Research*, Vol 15, No 1, pp 47-63

de Marsily G, 1986. Quantitative hydrogeology. Academic Press, San Diego, California

Domenico P A & Schwartz F W, 1990. Physical and Chemical Hydrogeology. John Wiley, New York

Elsworth D & Doe T, 1986. Application of non-linear flows laws in determining rock fissure geometry from single borehole pumping test. *Int. J. Rock Mech. Min. Sci. and Geomech. Abst.*, Vol 23, pp 245-254

Freeze R A, 1975. A stochastic conceptual analysis of one-dimensional groundwater in nonuniform homogeneous media. *Water Resources Research*, Vol 11, No 5, pp 725-741

Gale J E, 1993. Fracture properties from laboratory and large scale field tests: Evidence of scale effects. *Scale effects in rock masses 93*, Pinto da Cunha (ed), Balkema, Rotterdam

Geier J, Axelsson C-L, Hässler L & Benabderrahmane A, 1992. Discrete fracture modelling of the Finnsjön rock mass: phase 2. SKB TR 92-07

Gustafson G & Åberg B, 1985. Hydraulic conditions in caprock and reservoir. Vattenfall - deep gas project, internal report

Gutjar A L, Gelhar L W, Bakr A A & MacMillan J R, 1978. Stochastic analysis of spatial variability in subsurface flows 2. Evaluation and application. *Water Resources Research*, Vol 14, No 5, pp 953-959

Hakami E, 1988. Water flow in single rock joints. Licentiate Thesis, Luleå University of Technology, Luleå

Hakami E, 1995. Aperture distribution of rock fractures. Ph. D. Thesis, Royal Institute of Technology, Division of Engineering Geology, Stockholm

Hakami E & Larsson E, 1996. Aperture measurements and flow experiments on a single natural fracture. *Int. J. Rock Mech. Min. Sci. & Geomech. Abstr.*, Vol 33, No 4, pp 395-404

Kirkpatrick S, 1973. Percolation and conduction. *Rev. Mod. Phys.* Vol 45, pp 574-588

Maini T & Hacking G, 1977. An examination of feasibility of hydrologic isolation of a high level waste repository in crystalline rocks. Invited paper, Geologic Disposal of High Radioactive Waste Session, Ann. Meet, Geol Soc. Am., Seattle, Washington

Matanga G B & Frind E O, 1983. An evaluation of mathematical models for mass transport in saturated- unsaturated porous media. Atomic Energy of Canada Limited, TR-306.1983

Norman R M, 1990. Wettability and its effect on oil recovery. *Journal of Petroleum Technology*, Dec. 1990, pp 1476-1484

Olsson O, 1992. Site Characterization and Validation - Final Report. Stripa Project TR 92-22

Piggot A R & Elsworth D, 1993. Laboratory assessment of equivalent apertures of a rock fracture. *Geophys Res. Lett.* Vol 20, pp 1387-1390

Rasmuson A, 1978. Water flow in an unsaturated porous medium. Ph. D. Thesis, Royal Institute of Technology, Department of Chemical Engineering, Stockholm

Rasmuson A, 1989. Modelling of solute transport in the unsaturated zone. SNV Report 3592

Svensson U, 1992. On the relation between the effective conductivity and the standard deviation of the conductivity field Computer-aided. Fluid Engineering AB, Norrköping

Wikberg P, Gustafson G, Rhen I & Stanfors R, 1991. Äspö Hard Rock Laboratory. Evaluation and conceptual modelling based on the pre-investigations. SKB TR 91-22

Yortsos Y C & Fokas A S, 1983. An analytical solution for linear waterflood including the effects of capillary pressure. *Soc. of Petroleum Engineers Journal*, Feb. 1983, pp 115-124

Zimmerman R W & Bodvarsson G S, 1996. Hydraulic conductivity of rock fractures. *Transport in porous Media*, vol 23, pp 1-30

1 DESCRIPTION OF GEOBLOCK

1.1 INTRODUCTION

Geoblock is a computer code developed at the Department of Geology at Chalmers University of Technology, Göteborg. Geoblock is based upon the spreadsheet code Wingz and is primarily intended for flow-modelling in three dimensions with heterogenous conductivities. The code was developed within the Swedegas project in Dannemora. The code is, however, very general and is useful for all potential- and flow-problems which can be handled as a stochastic continuum in two or three dimensions.

1.2 THEORETICAL BACKGROUND

Geoblock is a finite difference model in three dimensions. Characteristic for the model is that it is possible to handle heterogenous conductivities in a simple way.

It is possible to calculate the connection between two cells in a couple of ways. The most common is with a discrete connection. Let us study two adjoining cells with apparent conductivities, K_n , and potential-levels, h_n .

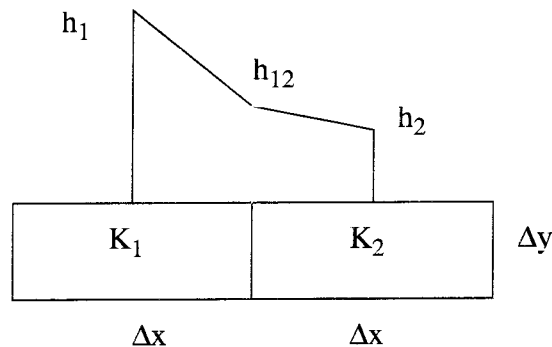


Figure 1-1. Two cells with potential-distribution.

The flow between the two cells can be written as

$$q = \frac{h_1 - h_{12}}{\frac{\Delta x}{2}} K_1 = \frac{h_{12} - h_2}{\frac{\Delta x}{2}} K_2 \quad (1)$$

Appendix 1:2

and we get

$$h_{12} = \frac{h_1 K_1 + h_2 K_2}{K_1 + K_2} \quad (2)$$

If we use this in equation (1) we can write it as

$$q = \frac{h_2 - h_1}{\Delta x} \frac{2K_1 K_2}{K_1 + K_2} \quad (3)$$

We can now write the relative conductivity:

$$K_{12} = \frac{2K_1 K_2}{K_1 + K_2} \quad (4)$$

and it is possible to calculate the pressure level in a cell according to the cells around it with utilization of the fact that the total-flow to the cell is zero at stationary conditions.

$$h_0 = \left(\sum_n h_n K_{0n} \right) / \left(\sum_n K_{0n} \right) \quad (5)$$

It is this relation which Geoblock is based upon. The code opens a worksheet with the model where the inner cells are related according to equation (5). Moreover it opens three conductivity sheets where the relative conductivities in each direction are stored.

1.3 MANAGEMENT OF GEOBLOCK

1.3.1 How to start Geoblock

To use Geoblock you must have the code Wingz and Geoblock installed. For installation of Geoblock, see chapter 1.4. To start Geoblock give the command `geoblock`, and Wingz will start automatically with the Geoblock-application.

Geoblock will first ask for a name of the current model, and if it is a new one or if it is an old one which you want to continue to work with.

When the code has the initial data it will open a couple of sheets. There are three conductivity sheets where the relative conductivity in each direction between two cells are stored. There is one worksheet where the potential for each cell is stored. It will also open one information sheet where information

to the user is recorded, e.g. where in the model the greatest change of the potential is. In this sheet some internal information for the code is also stored.

At the end of the initial session the code gives a menu where the functions in Geoblock are available.

1.3.2 Size of the model

To give the size and scale of the model, choose **Model-size** in the menu of Geoblock. The code will then open a window where you give the dimensions of the model in x, y and z direction and how many cells you want per unit of length. After that, the code first inserts the conductivity 1.0 in all conductivity cells and then equation (5) in the worksheet. The reason that the code put in conductivities first is that the cells in the worksheet will refer to the conductivities and then also in the denominator of the equation. If we do not give the conductivity any value we have to make a division with zero. All the border cells of the model are given the quality of a prescribed flux boundary. See chapter 1.3.3 for more information on the boundary.

To make it easier to manipulate the model, the code shades the inner cells with a grey color.

The code will also put some information in the information sheet to internal use, particularly for restarting the work with an earlier model.

1.3.3 Boundary conditions

It is possible to insert boundary conditions in the model in two different ways. You can either go to the worksheet and insert the value in the cells with the standard commands in Wingz, or use **Boundary-conditions** in the menu of Geoblock. The last one has the advantage that this function supports all the three dimensions of the model independently of the size of the model.

- Selecting boundary conditions with the **boundary**-function.

When you select the **boundary**-function in the menu of Geoblock the code opens a window where you can chose the options you want. The code does not care if it is inner or outer boundary conditions. The first thing to do here is to tell the code where the boundary is in the model. This you do by defining a box in the model where the boundary condition should be.

If the boundary condition is a constant head, i.e. Dirichlet's conditions, give the value of the head in the value box and click at OK.

If the boundary condition is described as a gradient of the head you should

Appendix 1:4

mark which coordinate direction the gradient is. The value box will now change and you can insert a start and end value of the gradient. Confirm by clicking at OK.

If the boundary condition is a no-flow boundary, i.e. Neumann's homogeneity conditions, mark in which direction, positive or negative regarding to the co-ordinate axis, the flow is. The value box will now disappear. Also one of the squares where the domain of the boundary is defined will disappear because it is now a section and not a box which should be defined. You can now click at OK.

- Selecting boundary conditions with standard commands in Wingz.

Zoom up the worksheet so you can see most of the model. It is now possible to insert boundary conditions in the model like any worksheet in Wingz. For more information, see the manual for Wingz.

1.3.4

Conductivities

The most important thing in Geoblock is the possibility to give the model heterogenous conductivities. To do that, select **Hydraulic properties** in the menu of Geoblock. The code will now open a window where you can select which value the conductivity should have and if it should be homogenous or heterogenous. If you select a heterogenous conductivity the code also needs a value of the variance of the log-normally distributed conductivity.

If you earlier had a log-normally distributed conductivity for the same model you can select to use the same random distribution but with new values on the mean and the variance.

When your selection is complete, confirm it by clicking at OK. The code will now calculate the new conductivities and insert the relative conductivities in each conductivity sheet. The normal distribution which has been used will be saved in a file with a suffix `norm`. It is this file Geoblock uses if you want new conductivities but with the same random distribution.

Geoblock shows in the information sheet values of the mean and the variance of the randomized conductivities. It is of course possible that this is not equal to the expected values, particularly for a small model.

It is also possible to make your own conductivity distribution or make changes in an old distribution. To do that, make a new file with the same name as the model and with the suffix `kond`. To insert the relative conductivities in each conductivity sheet, select **Hydraulic properties** in the menu of Geoblock and then **Recalc conductivity**.

1.3.5 **Iteration**

The automatic calculation of the value of the cells in the worksheet is disabled to make it faster to insert boundary conditions. Otherwise all cells should be recalculated every time a new value is inserted in the sheet. You must instead select **Calculation** in the menu of Geoblock and the code will open a window where you can specify how many times you want the code to iterate.

You have also the opportunity to select if you want Geoblock to report in which cell the greatest change was between the two latest iterations. To examine where this is will however take a while.

The result is written in the information sheet.

1.3.6 **Getting graphs**

When you select **Graph** in the menu of Geoblock, the code opens a window where you can select at which x, y or z coordinate you want to put the section for your figure. You should also specify if you want to have a figure of the potential or of the flow.

After you have confirmed it with OK the code opens an other sheet where the graph is done. You have now all the opportunities Wingz gives you to manipulate the graph.

If you want to save the figure, you must do it by yourself. Geoblock will not store it automatically when you exit. To save the figure you should select **save** under **file** in the Wingz menu.

1.3.7 **To end a session**

To end the session with Geoblock, select **Quit** in the menu of Geoblock. The code will save the model in the directory where you started it. However it will not save any graphs if you have not done it before, see chapter 1.3.6 above.

1.4 **INSTALLATION OF GEOBLOCK**

To install Geoblock you should do the following:

Log in as root

move to the directory were you have Wingz installed.

Appendix 1:6

```
cd destdir
```

Make a new subdirectory with name geoblock.

```
mkdir geoblock
```

Import the files `geoblock.in`, `menu`, and `Geoblock` to the new subdirectory.

Start Wingz and open the file `geoblock.in` as a hyperscript and change the line

```
BLOCKDIR="/usr/local/geoblock"
```

so it corresponds to your new subdirectory. Save the file and exit Wingz.

Add the following line to your `.cshrc` or your `.login` file

```
setenv BLOCKDIR /usr/local/geoblock
```

where `/usr/local/geoblock` corresponds to where you have `Geoblock`.

Import the file `geoblock` to `/usr/local/bin` or another suitable directory which is in your path.

1

MEASURED DATA

1.1

STEADY STATE FLOW MEASUREMENTS

Following tables are over measured flow trough the fracture. In the column Bottom are the water pressure head at the bottom of the core. Columns Head L and Head K are the water head in the two pressure measuring points.

Table 1-1. 0.30 MPa

Bottom [mm]	Flow [ml/s]	Head L [mm]	Head K [mm]	Calculated T [m ² /s]
2095	15.80	994	709	$1.64 \cdot 10^{-5}$
1612	12.90	771	561	$1.74 \cdot 10^{-5}$
1475	12.10	703	512	$1.78 \cdot 10^{-5}$
1346	11.45	638	465	$1.85 \cdot 10^{-5}$
1219	10.40	574	417	$1.85 \cdot 10^{-5}$
1097	9.55	513	371	$1.89 \cdot 10^{-5}$
978	8.65	455	328	$1.92 \cdot 10^{-5}$
Mean:				$1.81 \cdot 10^{-5}$

Table 1-2. 0.45 MPa

Bottom [mm]	Flow [ml/s]	Head L [mm]	Head K [mm]	Calculated T [m ² /s]
2095	14.90	966	713	$1.55 \cdot 10^{-5}$
1609	11.90	735	537	$1.61 \cdot 10^{-5}$
1474	11.00	675	489	$1.62 \cdot 10^{-5}$
1345	10.30	608	442	$1.66 \cdot 10^{-5}$
1220	9.60	549	397	$1.71 \cdot 10^{-5}$
1095	8.80	491	353	$1.75 \cdot 10^{-5}$
978	7.95	437	313	$1.77 \cdot 10^{-5}$
Mean:				$1.67 \cdot 10^{-5}$

Appendix 2:2

Table 1-3. 0.60 MPa

Bottom [mm]	Flow [ml/s]	Head L [mm]	Head K [mm]	Calculated T [m ² /s]
2095	13.90	939	692	$1.44 \cdot 10^{-5}$
1605	11.25	711	515	$1.52 \cdot 10^{-5}$
1472	10.40	651	471	$1.54 \cdot 10^{-5}$
1344	9.60	591	426	$1.55 \cdot 10^{-5}$
1217	8.85	532	382	$1.58 \cdot 10^{-5}$
1096	8.15	478	341	$1.62 \cdot 10^{-5}$
977	7.40	424	300	$1.65 \cdot 10^{-5}$
Mean:				$1.56 \cdot 10^{-5}$

Table 1-4. 0.75 MPa

Bottom [mm]	Flow [ml/s]	Head L [mm]	Head K [mm]	Calculated T [m ² /s]
2095	13.47	917	672	$1.40 \cdot 10^{-5}$
1609	11.05	698	504	$1.49 \cdot 10^{-5}$
1479	10.25	639	461	$1.51 \cdot 10^{-5}$
1349	9.40	581	417	$1.51 \cdot 10^{-5}$
1223	8.60	519	375	$1.53 \cdot 10^{-5}$
1096	7.90	469	333	$1.57 \cdot 10^{-5}$
976	7.15	415	295	$1.59 \cdot 10^{-5}$
Mean:				$1.51 \cdot 10^{-5}$

Appendix 2:3

Table 1-5. 0.90 MPa

Bottom [mm]	Flow [ml/s]	Head L [mm]	Head K [mm]	Calculated T [m ² /s]
2095	12.93	905	667	$1.34 \cdot 10^{-5}$
1603	10.15	689	501	$1.38 \cdot 10^{-5}$
1471	9.35	630	458	$1.38 \cdot 10^{-5}$
1342	8.60	572	415	$1.39 \cdot 10^{-5}$
1218	7.90	516	372	$1.41 \cdot 10^{-5}$
1096	7.40	463	332	$1.47 \cdot 10^{-5}$
975	6.55	411	293	$1.46 \cdot 10^{-5}$
Mean:				$1.40 \cdot 10^{-5}$

Table 1-6. 1.05 MPa

Bottom [mm]	Flow [ml/s]	Head L [mm]	Head K [mm]	Calculated T [m ² /s]
2095	11.20	892	649	$1.16 \cdot 10^{-5}$
1603	9.40	677	486	$1.27 \cdot 10^{-5}$
1471	8.75	619	443	$1.29 \cdot 10^{-5}$
1342	7.85	562	399	$1.27 \cdot 10^{-5}$
1215	7.15	506	359	$11.28 \cdot 10^{-5}$
1093	6.45	454	320	$1.28 \cdot 10^{-5}$
974	6.00	403	283	$1.34 \cdot 10^{-5}$
Mean:				$1.27 \cdot 10^{-5}$

Appendix 2:4

Table 1-7. 1.20 MPa

Bottom [mm]	Flow [ml/s]	Head L [mm]	Head K [mm]	Calculated T [m ² /s]
2095	10.50	871	627	$1.09 \cdot 10^{-5}$
1604	8.30	662	470	$1.12 \cdot 10^{-5}$
1470	7.70	606	429	$1.14 \cdot 10^{-5}$
1342	7.15	551	388	$1.16 \cdot 10^{-5}$
1216	6.65	498	349	$1.19 \cdot 10^{-5}$
1096	6.00	448	313	$1.19 \cdot 10^{-5}$
975	5.35	398	276	$1.19 \cdot 10^{-5}$
Mean:				$1.15 \cdot 10^{-5}$

Table 1-8. 0.45 MPa (II)

Bottom [mm]	Flow [ml/s]	Head L [mm]	Head K [mm]	Calculated T [m ² /s]
2094	11.50	928	672	$1.19 \cdot 10^{-5}$
1602	9.10	705	505	$1.23 \cdot 10^{-5}$
1472	8.50	646	461	$1.25 \cdot 10^{-5}$
1344	8.00	593	418	$1.29 \cdot 10^{-5}$
1215	7.15	531	375	$1.28 \cdot 10^{-5}$
1093	6.65	475	333	$1.32 \cdot 10^{-5}$
1090	6.50	472	327	$1.30 \cdot 10^{-5}$
976	5.90	417	295	$1.31 \cdot 10^{-5}$
Mean:				$1.27 \cdot 10^{-5}$

1.2

TRANSIENT FLOW MEASUREMENTS

Following tables are over the time response to a momentary change of the water head gradient. The water head at the bottom of the core was changed at time step 30.0 seconds.

Table 1-9. 0.75 MPa

Bottom [mm]	Flow [ml/s]	Time [s]
976	6.30	10.0
976	6.70	20.0
976	6.90	30.0
2095	8.20	40.0
2095	10.00	50.0
2095	11.20	60.0
2095	11.70	70.0
2095	11.60	80.0
2095	12.50	90.0
2095	13.20	100.0
2095	12.90	110.0
2095	12.80	120.0
2095	12.40	130.0
2095	12.70	140.0
2095	12.90	150.0
2095	13.20	160.0
2095	12.80	170.0
2095	12.80	180.0
2095	12.60	190.0
2095	12.70	200.0
2095	13.00	210.0
2095	13.30	220.0
2095	12.80	230.0

Appendix 2:6

Table 1-10. 0.9 MPa

Bottom [mm]	Flow [ml/s]	Time [s]
976	6.58	10.0
976	6.47	20.0
976	6.41	30.0
2095	7.94	40.0
2095	9.65	50.0
2095	10.85	60.0
2095	11.26	70.0
2095	11.53	80.0
2095	12.11	90.0
2095	12.67	100.0
2095	12.23	110.0
2095	11.88	120.0
2095	12.07	130.0
2095	12.17	140.0
2095	12.30	150.0
2095	12.68	160.0
2095	12.33	170.0
2095	12.22	180.0
2095	11.90	190.0
2095	12.28	200.0
2095	12.30	210.0
2095	12.79	220.0

Appendix 2:7

Table 1-11. 1.05 MPa

Bottom [mm]	Flow [ml/s]	Time [s]
976	5.69	10.0
976	5.75	20.0
976	5.71	30.0
2095	6.94	40.0
2095	9.04	50.0
2095	9.69	60.0
2095	9.70	70.0
2095	10.56	80.0
2095	10.93	90.0
2095	11.06	100.0
2095	11.20	110.0
2095	10.99	120.0
2095	10.65	130.0
2095	10.79	140.0
2095	11.00	150.0
2095	11.08	160.0
2095	11.20	170.0
2095	10.85	180.0
2095	10.58	190.0
2095	10.63	200.0
2095	10.95	210.0
2095	11.27	220.0
2095	11.35	230.0

Appendix 2:8

Table 1-12. 1.20 MPa

Bottom [mm]	Flow [ml/s]	Time [s]
976	5.27	10.0
976	5.07	20.0
976	5.15	30.0
2095	6.70	40.0
2095	8.40	50.0
2095	9.03	60.0
2095	9.16	70.0
2095	9.77	80.0
2095	9.68	90.0
2095	10.25	100.0
2095	10.18	110.0
2095	10.07	120.0
2095	9.70	130.0
2095	9.91	140.0
2095	10.09	150.0
2095	10.23	160.0
2095	10.42	170.0
2095	9.78	180.0
2095	9.84	190.0
2095	10.26	200.0

TECHNICAL SPECIFICATION OF EPOFIX

Epofix is produced by Struers, Valhøjs Allé 176, DK-2610 Rødovre/
København, Denmark. The following technical description of Epofix is from
Struers *Instructions for Use*, dated 1985.05.

Epofix is a cold-setting resin based on two fluid epoxy components. This resin is specially developed for mounting of irregularly shaped specimens and for impregnation of porous specimens, where low shrinkage and good mechanical properties in the cured state are required. Owing to its low viscosity, Epofix will penetrate into all pores and cracks of the specimen. After curing Epofix can be cut, ground, polished, drilled, etc.

The pot life of Epofix is approximately 30 minutes at 25°C.

As soon as the two liquid components have been mixed, the hardening process begins. Addition of smaller quantity of hardener than recommended will retard the reaction and prevent excessive generation of heat. However, deficiency of more than 10% provides a product which will never become completely hard.

An excessive quantity of hardener will promote the reaction. This reduces the processing time, but involves the risk that the mould may melt and that the specimen will become overheated.

Where considerable amounts of Epofix are used, the polymerization temperature may rise to such a level that it is necessary to eliminate the heat generated.

Epofix can be colored with Epodye to measure the porosity or with oil colors to achieve contrast.

Epofix has excellent adhesive properties and a very low shrinkage.

TECHNICAL DATA

Constituents	Liquid/liquid
Mixing ratio vol/vol	16/2
Mixing ratio weight/weight	18/2
Pot life	30 min (25°C)/15 min (50°C)

Appendix 3:2

Hardening time	8 hours (25°C)/2 hours (50°C)
Max. temp. during hardening	75°C
Linear hardening shrinkage	Insignificant
Hardness	74 Shore D
Vapour pressure	40 mm HG (25°C)
Viscosity	550 cp(25°C)/150 cp (50°C)
Refractive index	$n_D = 1.571$
Epofix resin, soluble in	Alcohol, acetone
Epofix hardener, soluble in	Alcohol, acetone, water
Resistant to	Acids, bases, acetone, alcohol
Cleaning of specimens	Specipur
Increase of hardness	Hardfiller
Moulds	Epoform

List of SKB reports

Annual Reports

1977-78

TR 121

KBS Technical Reports 1 – 120

Summaries

Stockholm, May 1979

1979

TR 79-28

The KBS Annual Report 1979

KBS Technical Reports 79-01 – 79-27

Summaries

Stockholm, March 1980

1980

TR 80-26

The KBS Annual Report 1980

KBS Technical Reports 80-01 – 80-25

Summaries

Stockholm, March 1981

1981

TR 81-17

The KBS Annual Report 1981

KBS Technical Reports 81-01 – 81-16

Summaries

Stockholm, April 1982

1982

TR 82-28

The KBS Annual Report 1982

KBS Technical Reports 82-01 – 82-27

Summaries

Stockholm, July 1983

1983

TR 83-77

The KBS Annual Report 1983

KBS Technical Reports 83-01 – 83-76

Summaries

Stockholm, June 1984

1984

TR 85-01

Annual Research and Development Report 1984

Including Summaries of Technical Reports Issued during 1984. (Technical Reports 84-01 – 84-19)

Stockholm, June 1985

1985

TR 85-20

Annual Research and Development Report 1985

Including Summaries of Technical Reports Issued during 1985. (Technical Reports 85-01 – 85-19)

Stockholm, May 1986

1986

TR 86-31

SKB Annual Report 1986

Including Summaries of Technical Reports Issued during 1986

Stockholm, May 1987

1987

TR 87-33

SKB Annual Report 1987

Including Summaries of Technical Reports Issued during 1987

Stockholm, May 1988

1988

TR 88-32

SKB Annual Report 1988

Including Summaries of Technical Reports Issued during 1988

Stockholm, May 1989

1989

TR 89-40

SKB Annual Report 1989

Including Summaries of Technical Reports Issued during 1989

Stockholm, May 1990

1990

TR 90-46

SKB Annual Report 1990

Including Summaries of Technical Reports Issued during 1990

Stockholm, May 1991

1991

TR 91-64

SKB Annual Report 1991

Including Summaries of Technical Reports Issued during 1991

Stockholm, April 1992

1992

TR 92-46

SKB Annual Report 1992

Including Summaries of Technical Reports Issued during 1992

Stockholm, May 1993

1993

TR 93-34

SKB Annual Report 1993

Including Summaries of Technical Reports Issued during 1993

Stockholm, May 1994

1994

TR 94-33

SKB Annual Report 1994

Including Summaries of Technical Reports Issued during 1994
Stockholm, May 1995

1995

TR 95-37

SKB Annual Report 1995

Including Summaries of Technical Reports Issued during 1995
Stockholm, May 1996

1996

TR 96-25

SKB Annual Report 1996

Including Summaries of Technical Reports Issued during 1996
Stockholm, May 1997

List of SKB Technical Reports 1997

TR 97-01

Retention mechanisms and the flow wetted surface – implications for safety analysis

Mark Elert
Kemakta Konsult AB
February 1997

TR 97-02

Äspö HRL – Geoscientific evaluation 1997/1. Overview of site characterization 1986–1995

Roy Stanfors¹, Mikael Erlström²,
Ingemar Markström³
¹ RS Consulting, Lund
² SGU, Lund
³ Sydkraft Konsult, Malmö
March 1997

TR 97-03

Äspö HRL – Geoscientific evaluation 1997/2. Results from pre-investigations and detailed site characterization. Summary report

Ingvar Rhén (ed.)¹, Göran Bäckblom (ed.)²,
Gunnar Gustafson³, Roy Stanfors⁴, Peter Wikberg²
¹ VBB Viak, Göteborg
² SKB, Stockholm
³ VBB Viak/CTH, Göteborg
⁴ RS Consulting, Lund
May 1997

TR 97-04

Äspö HRL – Geoscientific evaluation 1997/3. Results from pre-investigations and detailed site characterization. Comparison of predictions and observations. Geology and mechanical stability

Roy Stanfors¹, Pär Olsson², Håkan Stille³
¹ RS Consulting, Lund
² Skanska, Stockholm
³ KTH, Stockholm
May 1997

TR 97-05

Äspö HRL – Geoscientific evaluation 1997/4. Results from pre-investigations and detailed site characterization. Comparison of predictions and observations. Hydrogeology, groundwater chemistry and transport of solutes

Ingvar Rhén¹, Gunnar Gustafson², Peter Wikberg³
¹ VBB Viak, Göteborg
² VBB Viak/CTH, Göteborg
³ SKB, Stockholm
June 1997

TR 97-06

Äspö HRL – Geoscientific evaluation 1997/5. Models based on site characterization 1986–1995

Ingvar Rhén (ed.)¹, Gunnar Gustafson²,
Roy Stanfors⁴, Peter Wikberg⁴
¹ VBB Viak, Göteborg
² VBB Viak/CTH, Göteborg
³ RS Consulting, Lund
⁴ SKB, Stockholm
October 1997

TR 97-07

A methodology to estimate earthquake effects on fractures intersecting canister holes

Paul La Pointe, Peter Wallmann, Andrew Thomas,
Sven Follin
Golder Associates Inc.
March 1997

TR 97-08

Äspö Hard Rock Laboratory Annual Report 1996

SKB
April 1997

TR 97-09

A regional analysis of groundwater flow and salinity distribution in the Äspö area

Urban Svensson
Computer-aided Fluid Engineering AB
May 1997

TR 97-10

On the flow of groundwater in closed tunnels. Generic hydrogeological modelling of nuclear waste repository, SFL 3-5

Johan G Holmén
Uppsala University/Golder Associates AB
June 1997

TR 97-11

Analysis of radioactive corrosion test specimens by means of ICP-MS. Comparison with earlier methods

R S Forsyth
Forsyth Consulting
July 1997

TR 97-12

Diffusion and sorption properties of radionuclides in compacted bentonite

Ji-Wei Yu, Ivars Neretnieks
Dept. of Chemical Engineering and Technology,
Chemical Engineering, Royal Institute of
Technology, Stockholm, Sweden
July 1997

TR 97-13

Spent nuclear fuel – how dangerous is it? A report from the project "Description of risk"

Allan Hedin
Swedish Nuclear Fuel and Waste
Management Co,
Stockholm, Sweden
March 1997

TR 97-14

Water exchange estimates derived from forcing for the hydraulically coupled basins surrounding Äspö island and adjacent coastal water

Anders Engqvist
A & I Engqvist Konsult HB, Vaxholm,
Sweden
August 1997

TR 97-15

Dissolution studies of synthetic soddyite and uranophane

Ignasi Casas¹, Isabel Pérez¹, Elena Torrero¹,
Jordi Bruno², Esther Cera², Lara Duro²
¹ Dept. of Chemical Engineering, UPC
² QuantiSci SL
September 1997